UNIVERSITÀ DEGLI STUDI DI PADOVA

SCUOLA DI SCIENZE
Dipartimento di Geoscienze
Direttore Prof. Nicola Surian

TESI DI LAUREA MAGISTRALE IN GEOPHYSICS FOR NATURAL
RISKS AND RESOURCES

Deformation Processes in Carbonate-Built Faults During Seismic Slip

Relatore: Professor Giulio Di Toro
Correlatore: Dr. Stefano Aretusini

Laureanda: Kamyar Tamizkar
Matricola: 2070912

ANNO ACCADEMICO 2023-2024

Dedicated

Table of contents

Abstract

Earthquake ruptures often nucleate and propagate in carbonate-built terrains. This thesis investigates the mechanical behavior and microstructural/mineralogical evolution of carbonate faults during seismic slip in the presence of pressurized CO_2 and Argon (Ar). Using the SHIVA rotary shear apparatus, Carrara marble samples were subjected to high-velocity friction experiments to simulate natural seismic faulting conditions (e.g., slip rates of 6 m/s). The study aimed to understand how different gases influence fault mechanics, mineral transformations, and deformation mechanisms within the fault slip zone.

Compared to the experiment performed in pressurized Ar, the experiments conducted in pressurized CO_2 exhibited a lower peak friction coefficient and faster fault weakening, suggesting that CO_2 facilitates fault slip initiation. However, once the friction coefficient decays towards a minimum or steady-state condition, the frictional strength is negligible independently of the environmental conditions. The striking difference between the experiments performed in pressurized Ar and CO_2, is, in the latter case, the formation of a continuous < 0.3 mm thick visible black layer made of graphite or amorphous carbon (micro-Raman analysis).

Detailed SEM, cathodoluminescence, and EDS analyses of the samples recovered from the CO_2 and Ar experiments did not reveal significant microstructural differences within the slip zones. They are both < 0.1 mm thick and include ~ 1 μm in size particles of graphite wrapped by a continuous matrix made of sub-micron-in-size calcite grains. Instead, the micro-Raman investigation revealed the abundant presence of graphite/amorphous carbon on the slip surface of the experiment performed in pressurized CO_2. The identification of graphite is noteworthy as it may act as a solid lubricant especially at slip initiation, contributing to lowering the fault frictional strength in the experiments performed under pressurized CO_2. However, most of the observed graphite/amorphous carbon probably precipitated in a reduced environment (pressurized CO_2) during the late stages of seismic slip and subsequent cooling.

As a consequence, environmental conditions (this thesis: pressurized CO_2 or Ar; previous works: room humidity, vacuum, or pressurized H_2O, Violay et al., 2014)

contribute significantly to the evolution of fault frictional strength at the beginning of seismic slip. However, once seismic slip increases, the external environmental conditions have a limited role in controlling fault friction. In fact, the extremely low friction coefficient (or coseismic fault strength) is the result of temperature- and grain-size-dependent processes activated in the calcite-rich slipping zone. At this stage, the fault slip zone is a closed system and the "external" environmental conditions (presence of H_2O, CO_2, Ar, etc.) are irrelevant to the activation of particular deformation mechanisms. Instead, the "external" environmental conditions contribute to the particular mineral assemblage or amorphous phases that form during seismic slip deceleration and cooling after the slip event.

Riassunto

Le rotture sismiche spesso enucleano e si propagano in formazioni carbonatiche. Questa tesi indaga il comportamento meccanico e l'evoluzione microstrutturale/mineralogica delle faglie carbonatiche durante lo scivolamento cosismico in presenza di CO_2 e Argon (Ar) pressurizzati. Utilizzando l'apparato sperimentale SHIVA, campioni di marmo di Carrara sono stati sottoposti a esperimenti di attrito ad alta velocità per simulare le condizioni naturali di fagliazione sismica (ad esempio, velocità di slittamento di 9 m/s). La tesi mira a comprendere come i diversi gas influenzino la meccanica della faglia, le trasformazioni dei minerali e i meccanismi di deformazione all'interno della zona di scivolamento della faglia.

Rispetto all'esperimento condotto in Ar pressurizzato, gli esperimenti effettuati in CO_2 pressurizzata hanno mostrato all'inizio dello scivolamento un coefficiente di attrito di picco più basso e un indebolimento più rapido della faglia, suggerendo che la CO_2 facilita l'innesco dell'instabilità della faglia. Tuttavia, una volta che il coefficiente di attrito decade verso una condizione di minimo o di stato stazionario, esso è trascurabile indipendentemente dalle condizioni ambientali. La differenza più evidente tra gli esperimenti condotti in Ar pressurizzato e CO_2 è la formazione, in quest'ultimo caso, di uno strato nero e continuo di spessore < 0,3 mm costituito da grafite o carbonio amorfo (analisi micro-Raman).

Le analisi al SEM, alla catodoluminescenza e all'EDS delle zone di scivolamento degli esperimenti con CO_2 e Ar hanno mostrato che queste hanno spessore < 0,1 mm e comprendono particelle di grafite di dimensioni di ~ 1 μm avvolte da una matrice continua costituita da grani di calcite di dimensioni inferiori al micron. L'indagine micro-Raman ha invece rivelato l'abbondante presenza di grafite/carbonio amorfo sulla superficie di scivolamento dell'esperimento eseguito in CO_2 pressurizzata. L'identificazione della grafite è degna di nota in quanto potrebbe agire come lubrificante solido, soprattutto all'inizio dello scivolamento sismico, contribuendo a ridurre la forza di attrito della faglia negli esperimenti effettuati in CO_2 pressurizzata. Tuttavia, la

maggior parte della grafite/carbonio amorfo osservato è probabilmente precipitato in un ambiente riducente (CO_2 pressurizzata) durante le ultime fasi dello scivolamento sismico e il successivo raffreddamento.

Di conseguenza, le condizioni ambientali (questa tesi: CO_2 o Ar pressurizzati; studi precedenti: umidità atmosferica, vuoto o H_2O pressurizzata, Violay et al., 2014) contribuiscono in modo significativo all'evoluzione della resistenza di attrito della faglia all'inizio dello scivolamento sismico. Tuttavia, superata la fase iniziale di scivolamento, le condizioni ambientali esterne hanno un ruolo limitato nel controllo dell'attrito della faglia. Infatti, il coefficiente di attrito cosismico estremamente basso è il risultato di processi deformativi dipendenti dalla temperatura e dalla granulometria attivati nella zona di scivolamento ricca in calcite. In questa fase, la zona di scivolamento della faglia è un sistema chiuso e le condizioni ambientali "esterne" (presenza di H_2O, CO_2, Ar, ecc.) sono irrilevanti per l'attivazione di particolari meccanismi deformativi. Invece, le condizioni ambientali "esterne" contribuiscono alla particolare associazione di minerali e fasi amorfe che si formano alla fine dello scivolamento sismico e durante il successivo raffreddamento.

Chapter 1. Introduction

1.1. Earthquake in Carbonates

There are lots of definitions of what an earthquake is. For a general definition: Earthquakes are small to high-ground displacements that happen very quickly induced by the passage of seismic waves which are radiate from: 1. rupture propagation along faults (at km. s^{-1}) And 2. frictional interaction between the wall rocks bordering the fault during slip Earthquake (at m.s^{-1}) (Scholz 2002; Di Toro et al. 2010). The majority of data about the physics of earthquake sources are obtained through seismic wave inversion, interferometric synthetic aperture radar (InSAR) investigation, and other indirect geophysical methods (Scholz, 2019). However, to investigate the co-seismic processes, there are two complementary methods: 1- The use of experimental rock deformation machines, which are capable of simulating seismic slip conditions on a lab scale with the ability to control the experiment condition (Normal stress, velocity, acceleration, pore pressure, presence of CO_2 or other gases, etc.), and 2- investigation of ancient seismic faults and natural fault products currently exposed at the Earth's surface (Di Toro et al. 2009).

Several earthquakes in Italy, Greece, and also Iran surely propagate and in some cases are nucleated in Carbonate-dominated fault zones (Billi and Di Toro. 2008; Di Toro et al. 2010; Nissen et al. 2011). In fact, in many tectonically active regions, like the Mediterranean where the interaction of different tectonic plates results in complex seismic activity, carbonate rocks, such as limestone and dolomite, are very common (Fig. 1.1). As a consequence, the study of the deformation processes during seismic fault slip that occur in carbonates, especially given their quite unique physical and chemical properties, is crucial to understand earthquake mechanics in the densely populated areas.
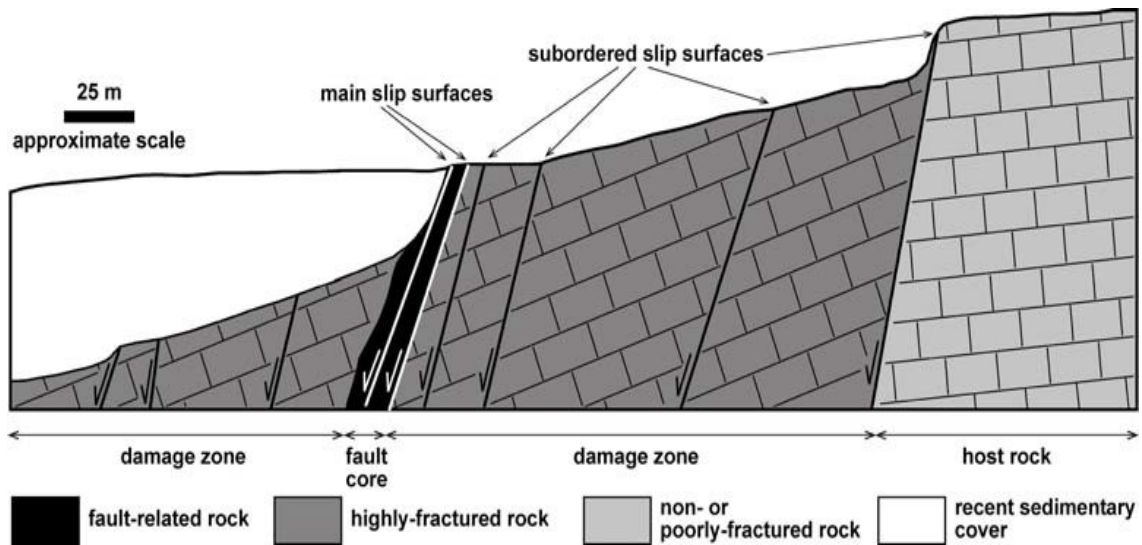
Figure 1.1 The figure shows a conceptual model of a typical fault zone in carbonate rocks, including a 1-fault core: where most of the displacement occurs. A 2-damage zone: where the carbonate rocks are highly fractured. A 3-host rock: where in most cases it remains poorly to non-fractured (adapted from "Billi and Di Toro. 2008, Fig.2" For details and explanations please refer to the main article).

The interplay between the structural characteristics, frictional behavior, and deformation mechanisms in carbonate fault zones has significant implications for understanding seismic activity. The unique properties of carbonate rocks, such as their susceptibility to frictional weakening and their interaction with fluids, make them critical to studying earthquake mechanics. The 2009 L'Aquila earthquake in central Italy, where the main faulting occurred within carbonate sequences, is a prime example of how laboratory studies can inform our understanding of natural fault systems (Di Toro et al., 2010).

To highlight how significant the role of carbonate rocks is in earthquake mechanics, we can get back to the 2009 L'Aquila earthquake in central Italy, where the main faulting occurred within carbonate sequences (Di Toro et al. 2010). Demurtas et al. (2016) produced microstructural and field observations from exhumed nearby faults (e.g., Vado di Corno Fault zone) cutting carbonates and found, that the microstructures closely match those produced in the experiments results emphasizing the value of laboratory studies in understanding natural fault systems.

The majority of data about the physics of earthquake sources are obtained through seismic wave inversion, interferometric synthetic aperture radar (InSAR) investigation, and other indirect geophysical methods(Kanamori and Brodsky 2004). However, to investigate the co-seismic processes, there are two complementary methods: 1- The use of experimental rock deformation machines, which are capable of simulating seismic slip conditions on a lab scale with the ability to control the experiment condition (Normal stress, velocity, acceleration, pore pressure, presence of CO_2 or other gases, etc.), and 2- investigation both ancient seismic faults and natural fault products that are currently exposed at the Earth's surface (Di Toro et al. 2009). For details on SHIVA please see chapter 2.1.

1.2. Deformation processes during earthquakes

One of the most important characteristics of carbonate rocks in fault zones, with respect to silicate-built rocks, is their diverse breakdown processes and frictional behavior under seismic deformation conditions. In fact, carbonates, with the increase of temperature in the fault slip zone associated with rapid seismic slip and frictional heating, may breakdown (i.e., in calcite, the decarbonation reaction with release of CO_2 occurs at ~800°C at 1-atm and room humidity conditions) and then deform by grain size and temperature-dependent processes (e.g., Spagnuolo et al., 2015). Instead, silicate-built rocks under the same loading conditions undergo to frictional melting of the rock-forming minerals (Sibson, 1975). Many experimental studies indicated that frictional melting can lead to significant weakening along the fault in the case of silicate-built rocks (e.g., Hirose and Shimamoto, 2005; Di Toro et al., 2006). Instead, experiments performed on carbonate-built rocks show early and abrupt reductions in friction during seismic slip, but without the occurrence of frictional melting (Han et al., 2010; Spagnuolo et al., 2015; De Paola et al., 2015). In silicate-built rocks, the development of a continuous molten layer acts like a lubricant, which reduces the friction coefficient, potentially facilitating the propagation of seismic rupture (Di Toro et al., 2006). The growth of a molten layer along a fault can significantly affect its stability during high-velocity slip (Hirose and Shimamoto 2005). In addition to frictional melting, fluid-rock

interactions are a major factor influencing the behavior of carbonate faults during seismic slip events ([Violay et al. 2013](#)).
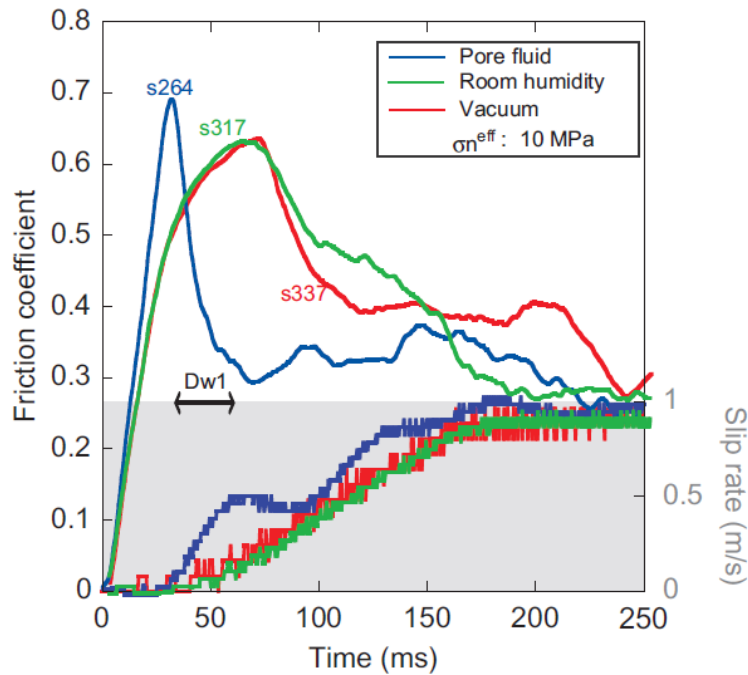

Figure 1.2 Violay et. al 2013, conducted experiments V=1 m/s and effective normal stress equals 10MP. The plot clearly shows the effect of pore pressure on the dynamic weakening of faults in comparison with room humidity or vacuum conditions (adapted from ([Violay et al. 2013](#), Fig. 4), For details and explanations please refer to the main article)

Violay conducted high-velocity friction experiments on Carrara marble, demonstrating that pore fluids could cause an abrupt reduction in fault strength. Under high pore pressure conditions, the friction coefficient dropped very quickly (Fig. 1.2), suggesting that pore pressure in fault zones could play a significant role in earthquake nucleation and propagation. These findings highlight the complex interaction between mechanical and chemical processes, particularly in carbonate-built faults, where fluid-induced weakening can be just as critical as thermal processes. The complexity of deformation in carbonate faults is also reflected in the diverse microstructures observed in fault rocks. These microstructures, which include features associated with dynamic recrystallization, cataclasis, and pressure solution processes, provide valuable insights into the conditions under which seismic slip occurs ([Delle Piane et al., 2017](#)).

Delle Piane et al., 2017 gathered all the potential microstructures obtained in experiments performed on calcite and dolomite-built rocks over a broad range of slip

rates, from sub-seismic (< 0.1 mm/s) to seismic (0.001-10 m/s), and summarized them in a figure (Fig 1.3). As indicated in the figure, diverse microstructures in carbonate rocks might occur at different slip rates. The microstructures are related to peculiar deformation mechanisms described by "frictional" constitutive laws which relate the dynamic fault strength to slip rate, normal stress, temperature, grain size, presence of fluids, etc. (Di Toro et al., 2011). As a consequence, the interpretation of microstructures may unravel the mystery of deformation happening during a seismic slip event and how the strength of a fault may evolve during the seismic cycle.
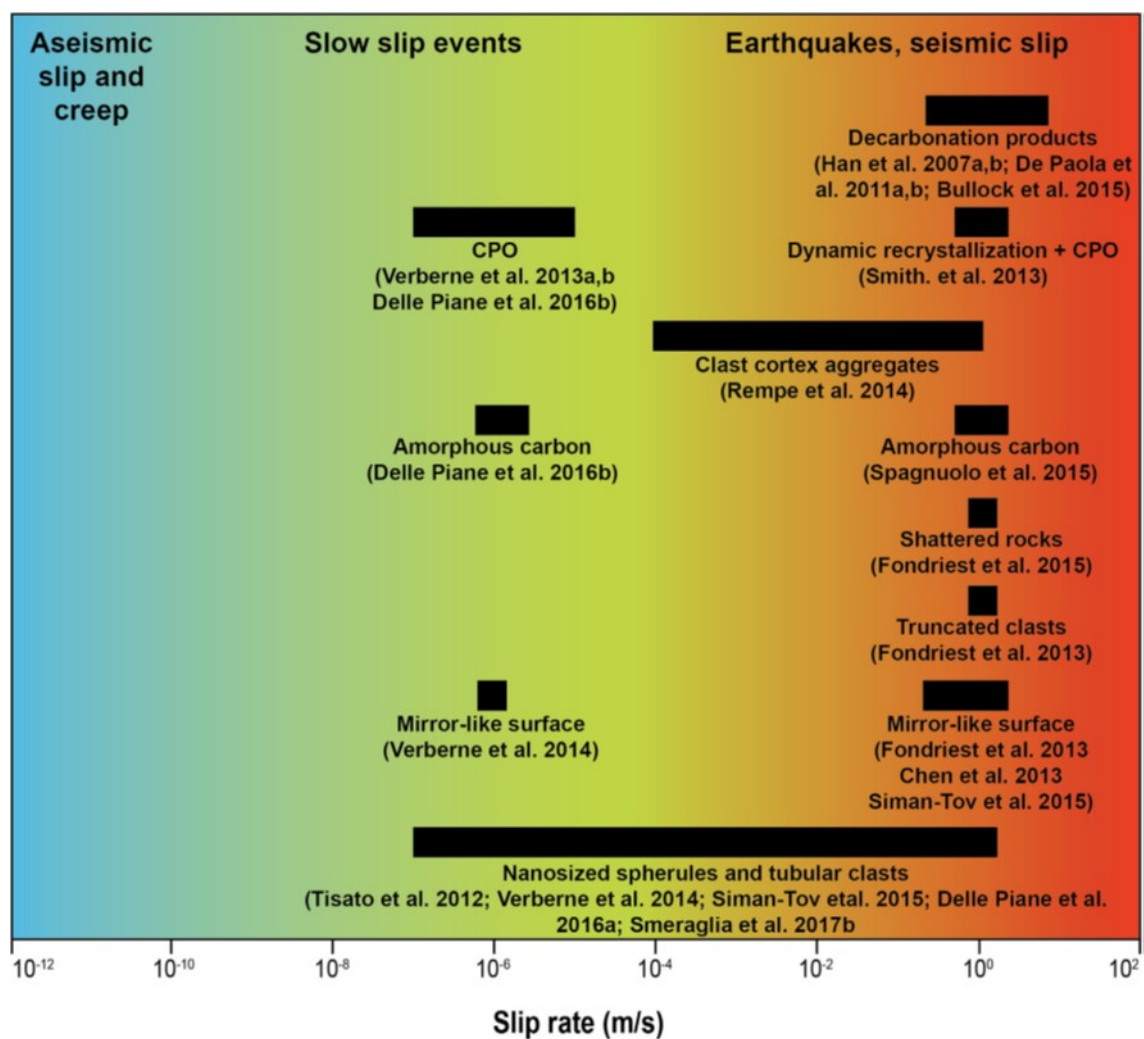

Figure 1.3 Potential microstructural seismic markers of carbonates according to slip rate (adapted from Delle Piane et al., 2017, Fig. 11, For details and explanations please refer to the main article)

Rocks on both sides of a fault are subject to significant stresses during an earthquake, engendering the type of deformation observed in fault zones.

Consequently, understanding the processes of deformation is important, since it is necessary to understand and predict how and why earthquakes occur and propagate, and to predict the ways that faults are likely to behave in the future. One of the most important mechanisms that previous studies showed is "frictional weakening". When rocks along both sides of a fault slide against each other at high velocities and accelerations this mechanism leads to a reduction in friction resistance along a fault plane. Previous studies showed that carbonate rocks are susceptible to this type of weakening mechanism. Han et al. (2007;2010) found that during seismic sliding, frictional heating can cause the thermal decomposition of calcite. This process leads to the formation of a thin layer of nanoparticles between the opposite fault surfaces that acts as a lubricant, reducing friction and allowing the fault to slide more easily (Pozzi et al., 2021; De Paola et al., 2015; Spagnuolo et al., 2015). However, the experiments were performed at room humidity conditions and there was no evidence for frictional melting. Instead, in silicate-built rocks (granite, gabbro, etc.), dedicated experiments performed at high rates of slip showed that severe frictional heating could cause these rocks to melt (Tsutsumi and Shimamoto, 1997; Hirose and Shimamoto, 2005; and Di Toro et al., 2006). This melt, which is akin to the lubricating layer that forms from thermal decomposition, substantially reduces the frictional resistance, causing the fault to slide even more readily. This is particularly important in faults that move quickly and over large distances during an earthquake. Lithology, pressure and temperature conditions, and fault maturity, are among the major parameters that can influence deformation processes in carbonates.

The deformation of faults is also influenced by fluid-rock interactions(Delle Piane et al. 2017). previous studies indicated that pore fluid can result in an abrupt decrease in fault strength. When slip occurs, these fluids that are trapped in the rock's pores experience high pressure, weakening the rock and encouraging fault movement (Violay et al. 2013). Understanding the relationship between fluids and rock is essential to comprehending the initiation and crustal propagation of some earthquakes. According to Billi (2010), calcite can fracture and undergo cataclastic flow at low grades (lower temperatures and pressures). This is often accompanied by intra-crystalline plastic

deformation, which manifests as twinning and crystal lattice straining. At temperatures below roughly 400 ℃, mechanical twinning in calcite is thought to be the predominant crystal-plastic deformation mechanism, occurring along the e-planes at critical resolved shear stresses as low as 2 MPa.

In carbonate faults, superplastic deformation and sliding at the grain boundary are two additional deformation mechanisms seen(Ashby and Verrall 1973; De Paola et al. 2015). According to Spagnuolo et al. (2015), grains in carbonate rocks can glide past one another more readily under high pressures and temperatures.

Rempe et al. 2017 performed several experiments using SHIVA at INGV in Rome (Italy) and pressurized high-velocity apparatus (Phv) at Kochi (Japan) on synthetic calcite gouges under room-dry and water-dampened conditions. Their findings show that, the presence of water significantly influences strain localization within calcite fault gouges during seismic slip. their experiments show that under room-dry conditions, calcite gouges show a prolonged strengthening before dynamic weakening. Despite this, under water-dampened conditions, they observed a nearly instantaneous reduction in friction (dynamic weakening) to a steady state condition which was also a bit higher than in room-dry conditions. Mitchell et al. (2015) discussed how the compaction and dilation of gouge material (fined-grain material which is very common in fault zones) during seismic slip can impact fault stability. The gouge can dilate, allowing for more movement and reducing friction, or compact, increasing friction and preventing further slipping, as the fault slips. The overall deformation of the fault during an earthquake can be greatly influenced by the balance between these processes. Fracturing and grain boundary processes also might be one the most dominating deformation mechanisms in carbonate-built faults. seismic slip may be the cause of fracture patterns and grain boundary sliding in the fault rock (Nielsen et al. 2021). These processes are essential to our knowledge of seismic events in carbonate-built fault zones because they contribute to the overall weakening and deformation of the fault during an earthquake.

Previous studies that tried to determine the deformation mechanisms that control dynamic fault weakening in carbonate-built faults revealed that (1) frictional

weakening is the result of a combination of different deformation mechanisms and (2) frictional melting in carbonate has never been observed (Spagnuolo et al., 2015; Dalle Piane et al., 2017).

1.3.   How the Thesis contributes all

This research dives deep into the hidden world of earthquakes, particularly in carbonate-rich zones like Italy, Iran, and Greece. We used cutting-edge tools, the SHIVA apparatus, and gets benefits of micro-Raman spectroscopy tools and also SEM (Scanning Electron Microscope), to get a close-up look at the main deformation processes that occurred in carbonate-built faults during seismic slip. We were particularly curious about how different environmental conditions (e.g., gases trapped within these rocks) might affect their frictional behavior. The presence of pressurized CO_2 can disrupt the regular molecular arrangement of the calcite crystal lattice which is caused by reducing the energy required to break the bond and initiate the melting (Durand, Baumgartner, and Marquer 2015). It is known from previous (petrological) studies that melting can occur when:

1.   confining pressures (normal stress) are 2700 MPa, at temperatures of 1610°C (no CO_2) to 1505°C (11.5 wt% CO_2) (Huang and Wyllie, 1976)

2.   confining pressures (normal stress) are 10000 MPa, at temperatures of ca. 1727°C (Osinski and Spray, 2001).

Passelègue et al. (2019) suggested that in carbonate, the presence of CO_2 dramatically lowers the melting point, potentially leading to melting at the asperity scale (Passelègue et al. 2019; Wyllie 1965).

In the study to see how much the gas composition mattered, we also performed experiments with the presence of pressurized Argon gas. We used Ar gas due to the very low chemical reactivity, also with carbonates under the explored deformation conditions. By carefully recreating the intense conditions of an earthquake in the laboratory, we describe how carbonate rocks react to seismic stress. We discuss how

the presence of CO_2 can affect the friction coefficient and how it would decrease during slip.

This research is not just about adding to our scientific knowledge. It has real-world implications. By better understanding how earthquakes happen in areas with carbonate rocks, we can improve our ability to predict and prepare for these events, potentially saving lives and protecting communities.

Chapter 2. Methods

In this chapter of the thesis, I describe sample preparation for experiments conducted with SHIVA, the experimental methodology, sample preparation for micro-Raman analysis, and the analysis conducted with micro-Raman and scanning electron microscope (SEM). Some of these methodologies were designed and implemented for this thesis and might not apply to other experimental setups.

2.1. SHIVA experimental machine

Four experiments we conducted with the SHIVA machine (Slow to HIgh Velocity Apparatus) designed and developed by Di Toro and installed at the National Institute of Geophysics and Volcanology in Rome, Italy (INGV) on November 20, 2009 (Fig. 2.1a). SHIVA offers researchers a state-of-the-art tool that is specifically designed to study the behavior of various rock types in a lab setting under controlled conditions at sub-seismic to seismic fault slip rates (from 10 μm s^{-1} to 6.5 m s^{-1}) and extraordinarily large acceleration (from 0 to 6.5 m s^{-2} in 0.1 s).

SHIVA is about 4 m long, 1 m wide, nearly 1.8m high, and 4 tons in weight (Di Toro et al., 2010). The setup of the machine is horizontal. The machine is fixed on a reinforced concrete foundation to minimize vibration and enhance the accuracy of the measured shear and normal stresses. The main parts of SHIVA include:

1. **Rotary side:** it includes one small (5.15 kW) and one large (up to 300 kW) brushless motors, a rotary shaft, angular encoders (to measure angular rotations), a gearbox that attaches the small engine to the rotary shaft, and a sprag clutch that connects the large motor to the rotary shaft (Right side in Fig. 2.1a)

2. **Sample chamber:** The sampler holder of SHIVA is designed for cylinders with an external diameter of 50 mm and an internal diameter range from 0 mm (solid cylinders) to 40 mm (hollow cylinders). The metal sample holders along with the soft aluminum rings put together to ensure a tight grip on the samples without subjecting the samples themselves to excessive force (Fig 2.1b). Additionally, the chamber is

equipped with a pressure vessel and a vacuum pump to perform experiments under environmentally controlled conditions (of N_2, CO_2, Ar, etc.). The chamber is connected to a mass spectrometer, to detect gas emitted from the sample (Spagnuolo et al., 2015). In the experiments conducted for the current thesis, some changes were made to the connection between the mass spectrometer and the chamber to install a pressure gauge to measure the gas pressure in the chamber to ensure that a fully pressured environment was achieved (Fig 2.1b).
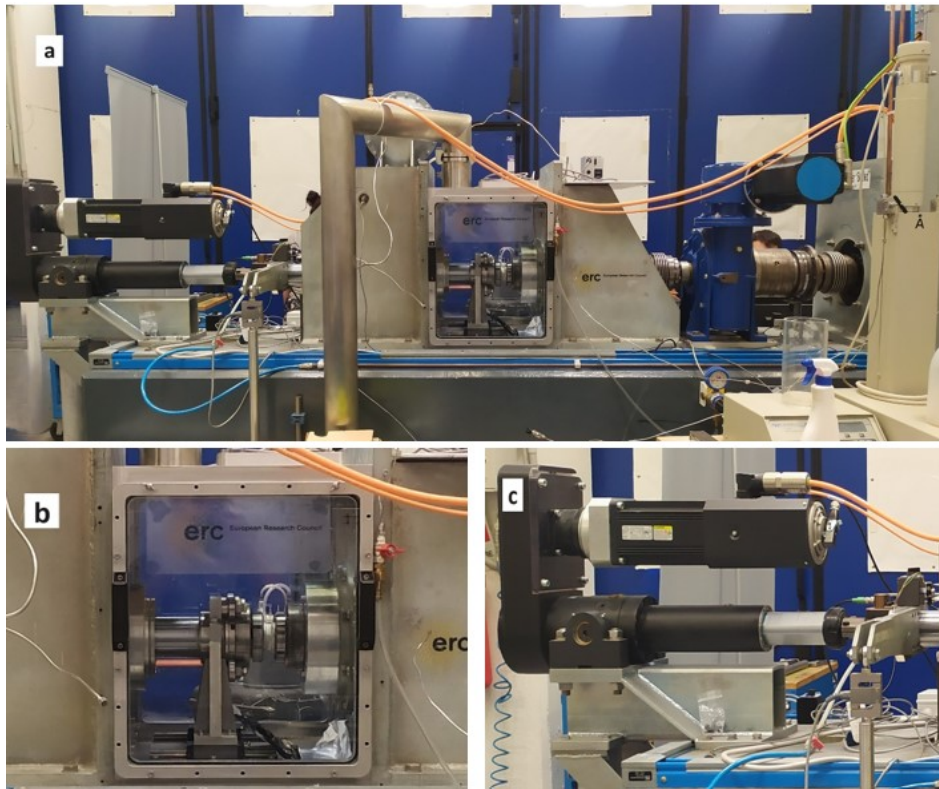

Figure 2.1 Figure includes: a: The SHIVA apparatus installed at the INGV Rome in HPHT lab. b: The sample Chamber of the SHIVA with samples on. In the picture, the rotary side is on the right. c: the electro-mechanical cylinder that controls the normal force on the sample.

3. **Axial side:** The maximum load that SHIVA can apply, considering the installed electromechanical cylinder, is rated to 68 kN. The axial side of SHIVA also includes an arm equipped with a load cell to measure torque, while another load cell on the axial column measures normal stress. The precise calibration of these components ensures accurate measurement and control, critical for experiments requiring high precision and stability under varying loads.

In "table 1" I put all the specifications and mechanical data of the SHIVA apparatus. For details related to the design and performance of the SHIVA please refer to (Di Toro et al. 2010; Aretusini et al. 2021).

SHIVA			
Weight (kg)		4,000	
Length (m)		4	
Height (m)		1.8	
Width (m)		1	
Max load (kN)		50	
Small motor		**Large motor**	
Power supply (V)	380	**Power supply (V)**	480
Peak power (kW)	5.15	**Peak power[1] (kW)**	280
Max torque (Nm)	4,500	**Max continuos power (kW)**	40
Slip rate range[2] (m s^{-1})	0.01-3	**Slip rate range[2] (m s^{-1})**	0.001-9
[1] For > 60s [2] For the samples with 50/40 Ext/Int in diameter		**Max torque at 1,800 RPM (N m)**	932
		Max torque at 3,000 RPM (N m)	437
		Max acceleration (m s^{-2})	80

Table 2.1 Specification and performance of the SHIVA. For more details, please refer to "Di Toro et al. 2010"

Experiments that are conducted with rotary shear machines (like SHIVA) might be challenging due to several factors, (1) a high relative slip rate (up to 6.5 m s^{-1}), (2) a large relative displacement (up to several meters), (3) high normal stress (up to 50 MPa) that is imposed onto a pair of cylindrical samples. Additionally, during the experiments, several variables should be monitored and recorded, for instance, the dynamic

evaluation of shear stress, shortening of the samples, slip rate, acceleration, and possibly other variables like temperature, and gas emissions (Di Toro et al. 2010; Spagnuolo et al. 2015; Aretusini et al. 2021). To address all of these challenges one of the most important key parameters is that the pairs of the samples be perfectly matched, aligned, and rectified to a tolerance of a few tens of micron or even less which this amount of precision require very careful preparation of the sample.

The first step of the preparation is choosing a slab, with perfectly parallel surfaces. The rock slab that we chose is made of Carrara marble "Statuario" type, about 99% calcite, and minor quartz, dolomite, and muscovite (Spagnuolo et al., 2015). The Pycnometer analysis revealed that the porosity of the chosen slab is 3.6398% (table 2.1). Using a rock coring machine and a core bit (Fig 2.2b-c), we drilled the slab to extract a cylindrical sample with about 50 mm in external diameter (Fig 2.3a). During this step, some of the samples were fractured due to the presence of micro-fractures inside the slab. The shape of some samples was not appropriate (not fully cylindrical) (for instance look at Fig. 2.3a). To solve this issue, we later lathed the outer edge into a perfect cylinder. This step took a lot of time and considerably reduced the external diameter by 1 to 2 mm.

In the previous sample preparation step, I also extracted a smaller sample from the main rock to perform a pycnometer analysis. To make the powders for the pycnometer, we used a mortar and used the 75 µm sieve to obtain as much as small and uniform calcite particles. After the pycnometer analysis, we calculated the porosity of the slab that we used with the assumption of having a uniform porosity across the slab (see calculation below in Table 2.2). Calculating porosity is important somehow, as it can significantly affect the dynamic weakening behavior of the carbonates during seismic slip as the greater the porosity, the more fluid is exposed to be pressurized (Nielsen et al. 2021; Violay et al. 2013).

Samples	Weight (gr)	Average Volume (cm³)	Average Density (g cm⁻³)	Variance (%)
Powder Calcite	2.4050	0.8540	2.8161	0.0442
Solid Calcite	98.5730	36.3258	2.7136	0.0067

Table 2.2 Pycnometer measurement report of both powder and solid calcite extracted from the main slab.

To calculate the porosity, we used the general formula:

$$Porosity = \left(1 - \frac{Bulk\ Density}{Particle\ Density}\right)$$

(Equation 2.1)

Given that the "bulk density=solid calcite density" and "particle density=powder calcite density" we have:

$$100 = 1 - \frac{2.7136}{2.8161} \times 100$$

Finally, we get porosity as:

Porosity=3.6398 %

The sample preparation continued by wrapping a zip tie close to the top of the sample to fix the height of the sample that needs to remain exposed at the top (for most samples around 3-5 mm remain exposed). With latex gloves and rubber rings, we sealed the bottom of the aluminum jacket to prepare them to pour the mix of epoxy resin and gravel (the latex gloves are used to avoid any leaking after pouring the resin). After pouring the prepared epoxy resin mixture inside the jacket, we pushed the samples into the metal ring to the desired height. This step requires a little bit of experience and care to be sure that the bottom of the sample is fully filled by the epoxy resin. One way to check this is that after pushing the sample into the aluminum rings, the cylindrical rock inside the jacket would mold floats. For the experiments with rotary shear machines, the tightness is very important. For this reason, we leave the prepared samples for 48 hours to fully cure to allow perfect solidification of the epoxy resin.
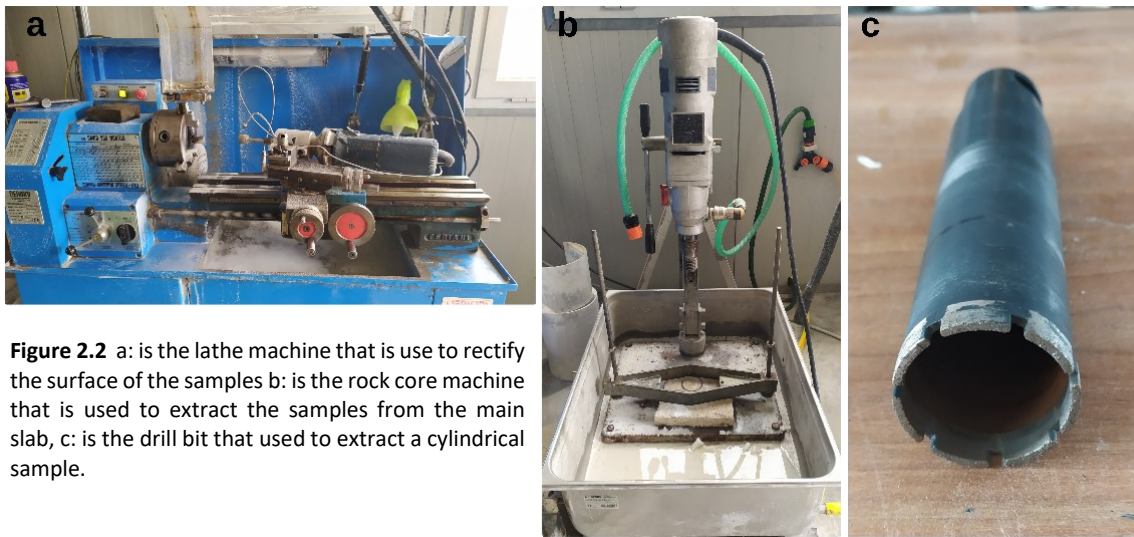
Figure 2.2 a: is the lathe machine that is use to rectify the surface of the samples b: is the rock core machine that is used to extract the samples from the main slab, c: is the drill bit that used to extract a cylindrical sample.

The next step of the sample preparation is to use a lathe machine to clean (a few micro-meters) and flatten the surface of the sample. Some resin on the surface of the exposed sample was eliminated with the lathe machine. The last step of the sample preparation is to make a hollow circle at the center of the sample (Fig 2.3c). This hollow-like circle is to determine better the mechanical data: in fact, in solid cylinders, the slip rate is nominally zero at the core and increases with the radius. Using hollow cylinders allows the experimentalist to obtain better measurements of the slip and slip rate. In total I prepared 6 pairs of samples (12 cylinders) of Carrara marble ("solid Calcite" in the following text), and as we wanted to perform at least 4 experiments also for reproducibility. One couple of cylindrical ("hollow Calcite" in the following text) were prepared starting from a 30/50 hollow Carrara marble core according to the procedure in Nielsen et al., (2012)
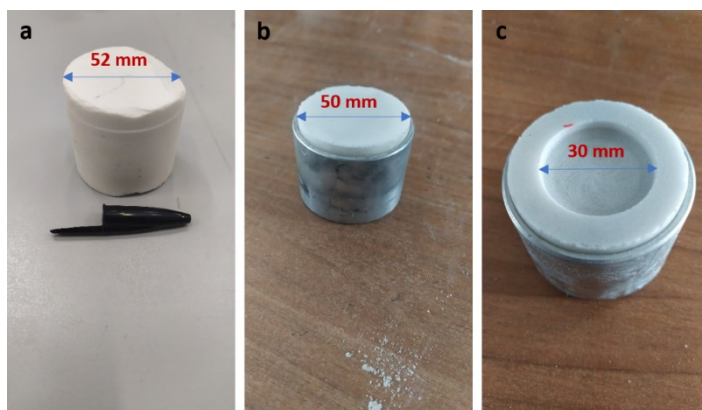

Figure 2.3 (a) raw cylindrical sample after extracting from the main slab, **(b)** fully cured rectified sample, 48 hours after pouring the epoxy resin mix and using the lathe machine to rectify the surface, **(c)** same sample after using the lathe machine to create a semi-hollow cylindrical sample.

After working and completing the samples for the experiments, we prepared the sample chamber of SHIVA. In total, we planned to conduct experiments with pressurized CO_2 and Ar gas. To reach pressurized conditions and avoid air/room humidity contamination that might affect our experimental and microanalytical data, we first evacuated the air from the chamber and reached a threshold vacuum pressure. To do this, after examining all the connections to prevent any leakage, we used the vacuum pump connected to the SHIVA. After checking possible leakages, we eventually succeeded in keeping the vacuum of the chamber in the range that is acceptable for our experiments (vacuum pressure should be lower than $2 \times 10^{-2}\ psi$). One of the possible leakage sources was the connection between the chamber and the mass spectrometer. Having the mass spectrometer connected to the chamber during the experiment is crucial as we can monitor the chamber for any contamination and ensure the presence of pressurized gas (CO_2 and Ar) inside the chamber. A detailed designed sketch of the SHIVA's chamber connection (Valves, Pressure gauges, flowmeter, etc.) can be found in Fig 2.4. This design allowed us to (1) monitor the vacuuming process, (2) make sure about the injection pressure of the gas (CO_2 or Ar) (3) monitor the pressure inside the chamber during the injection and make sure about the pressurized condition (4) monitor the chamber for any contamination and possible leakage. Additionally, before each experiment and installing samples in the chamber, we cleaned the chamber and all the instruments inside the chamber with alcohol to avoid contamination. In almost all the experiments the procedure was as follows (look at Fig 2.4 for the connection and locating the valves and Pressure gauges):

1. Cleaning inside the chamber and sample holders and all tools
2. Put the sample inside the sample holders (Fig 2.5a)
3. Starts the vacuum pump to reach at least $2 \times 10^{-2}\ psi$
4. Stop the vacuuming, then open the gas injection valve and read the pressure from the M1 gauge, we put the inlet pressure on 3 bar, and we then opened the V_1 valve to let the gas flow from the gas bottle to the chamber.
5. After nearly 1 and a half hours, we opened the V_2 valve and read the chamber gas pressure through M2.

6. Open V_3, fix the flowmeter, and read the Mass spectrometer data

7. Continued the mass spectrometer with V_1, V_3 open, and V_2 close and let them balance for 15 minutes. During this step, we were able also to look for any possible leakage.

8. Closed V_1 and V_3

9. Load the piston with a maximum target of 25 kN with rate of 5 kN min^{-1}

10. Set the slip rate and displacement target to 6 m s^{-1} and 6 m respectively, except in the s2013 experiment at which the target displacement was 20 m.

11. After the experiment, unload the piston and get a sample of the gas in the chamber for further analysis.

12. The last step is to carefully open the chamber, take the samples off carefully without any possible damage, especially to the surface of the samples, and collect the powders produced in the experiments for further analysis.

During experiments "s2013" and "s2019", we had axial piston oscillations after around 0.6 m of displacement, which induced damage to the surface of the sample. However, 0.6 m displacement was almost enough to reach "steady-state" conditions (that is, dynamic friction remains almost constant with slip distance).

After the experiments, we collected the samples for further analysis. Data acquisition (normal stress, shear stress, axial shortening, temperature, etc.) was at 25 kHz.
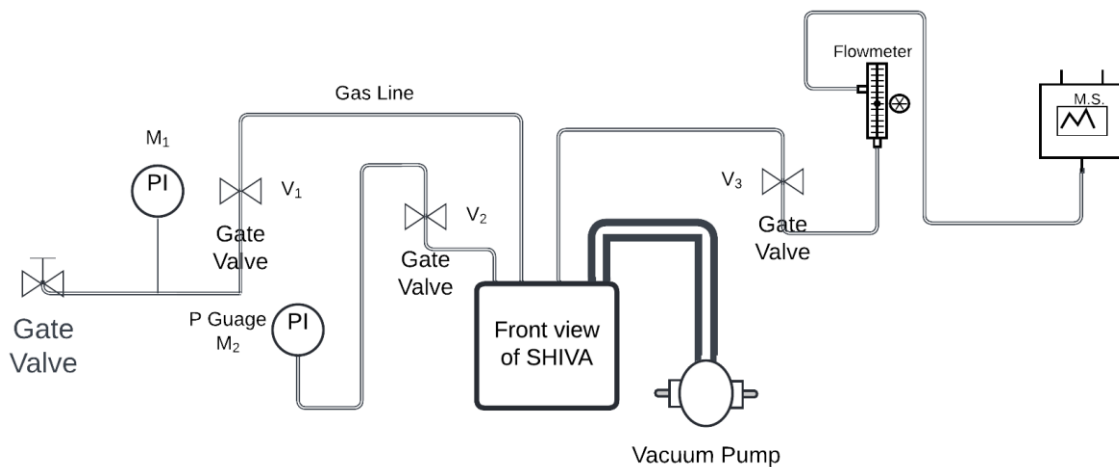

Figure 2.4 Drawing sketch of the SHIVA's chamber connection that designed for this thesis.

In total, we conducted 7 experiments with SHIVA. Four of these experiments were successful, generating a robust data set for further analysis (see Table 2.3)
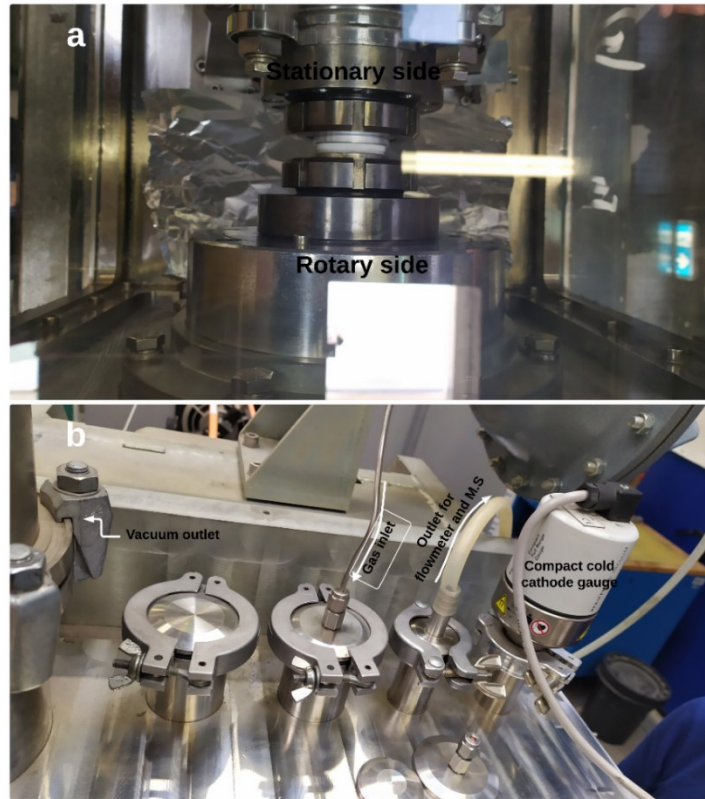

Figure 2.5 (a) Inside the chamber after putting samples on, (b) picture showing the top view of the chamber where all the connections connected to the chamber.

Experiment	S2013	S2016	S2017	S2019
Sample	Solid Calcite	Hollow Calcite	Solid Calcite	Solid Calcite
Inner diameter	30.32	30	30	29
Outer diameter	50.50	50	50	49
$\sigma_{n,t}$ (MPa)	20	20	20	20
V_t (ms^{-1})	6	6	6	6
δ (m)	20	6	6	6
Condition	CO_2	CO_2	Ar	CO_2

Table 2.3 Summary of all successful experiment conditions. Acronyms and symbols: $\sigma_{n,t}$= target normal stress, V_t=Target slip rate, δ=Displacement.

2.2. Micro-Raman

To study the deformation in carbonates, the key parameters is to understand any alteration in mineralogy and material's structure within the microscopic scale(Hope, Woods, and Munce 2001; Rividi et al. 2010; Tlili et al. 2002). The micro-Raman analysis is a powerful technique that allows researchers to investigate and study many aspects of geological sciences such as mineral phases, fluid inclusion, study alteration in mineralogy, morphology, crystallinity, etc. Unlike any other spectroscopy technique, micro-Raman analysis can provide non-destructive, stress-state, mineral phase transformations inside the rock sample (Buehn et al. 1999; Urashima et al. 2023). This technique is beneficial for analyzing and identifying any contamination or distribution of any specific mineral or material in a heterogeneous sample(Schmid and Dariz 2015). with this method, we can identify materials from their unique spectral fingerprints (a series of sharp peaks and troughs) using the library of known spectra.

For this study, the micro-Raman analysis was engaged to investigate any mineralogical or structural change within the surface of the sheared sample. We aim to investigate any specific mineral phases that are present after deformation and correlate them to the mechanical behavior observed during the experiments conducted with SHIVA.

After completing all the experiments with SHIVA and collecting the deformed samples one of the most important steps was to preserve the surface of the samples to avoid any further damage and alteration. Unfortunately, due to the piston instability during the s2013 and s2019 experiments, especially after 0.6 m of displacement, the surface of the samples was not preserved. Instead, the slip surfaces of s2016 and s2017 were recovered and we used a rock chisel to cut small pieces and use them for Raman analysis. All the results from the micro-Raman analysis can be found in Chapter 3, section 2.
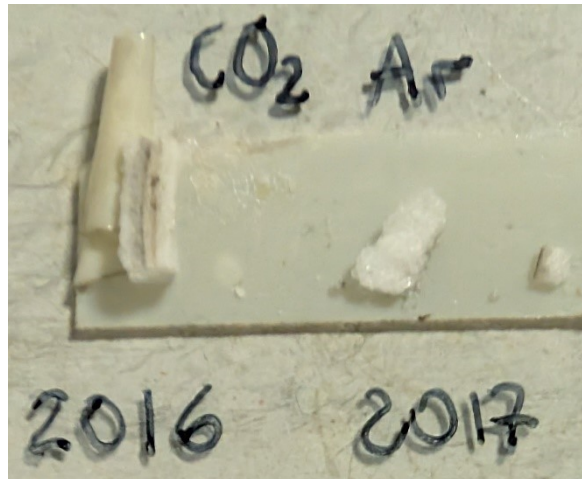
Figure 2.6 Samples collected from the slip surface of the s2016 and s2017 experiments for micro-Raman analysis.

In our experiments, micro-Raman analysis were performed with the WITec Alpha 300R confocal microscope with a XYZ motorized stage, equipped with a 532 nm laser diode installed at the Department of Geoscience at the University of Padova. Regarding the micro-Raman scan, the analyzed surface covered an area of 50x2000 μm^2, with a scanning density of 25 points/line and 1000 lines/image, under a laser power of 5.123 mW, with a scan speed of 0.02 lines/s over a spectral range from 40 to 3900 cm^{-1}. Raman spectra were recorded with an integration time of 2 s and the data was acquired with a grating of 300 groove/mm. Data was analyzed using WITio, a free script-based MATLAB data evaluation toolbox.

2.3. Scanning Electron Microscope

Scanning electron microscope (SEM) is a valuable and powerful technique in geological sciences as it can used to produce detailed pictures of rock surfaces down to a resolution of few nanometers. These high-magnification and high-resolution images allow researchers to study microstructural features such as grain size, nano-scale porosity, fracture network, etc., down to the nanoscale. So SEM observations are pivotal to understanding the deformation mechanism that occurs in fault slip zones during seismic slip (Collettini et al. 2013; Spagnuolo et al. 2015; Siman-Tov et al. 2013). To prepare the samples for SEM, from each pair of samples, one was preserved for micro-

Raman analysis and the other sample was conserved for scanning electron microscope (SEM) analysis. The latter parts of the samples were embedded with low-viscosity resin (Araldite 2020, a two-component low-viscosity, water white adhesive, clear epoxy system composed of XW 396 resin and XW 397 hardener) for consolidation and polishing for SEM observations. The specimens were carefully polished in with increasing grit sandpaper (800,1200,2400, and 4000) to obtain a mirror-like ultra-polished surface. Note that other than the initial cut of the sample that was done with a diamond saw cooled with water, all the other steps were conducted with oil to avoid contamination and alteration of the delicate water-reactive (e.g., CaO) that may have formed in the experiments in the slip zone and nearby. This sample preparation procedure took several days because performed by hand and very slowly to avoid scratching of the sample surfaces (Fig 2.7).
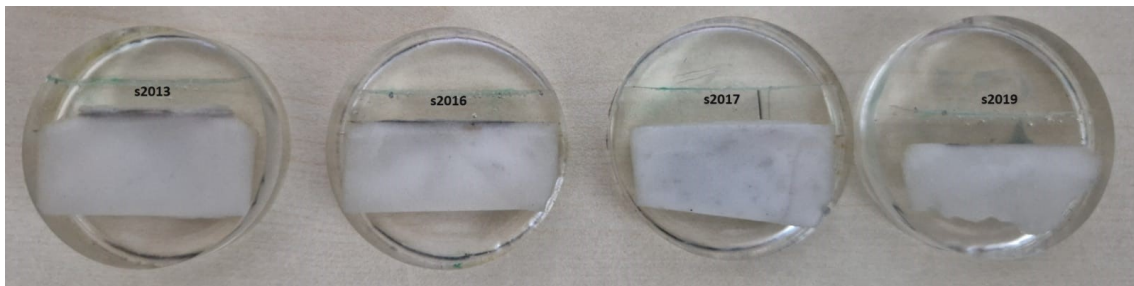

Figure 2.7 The samples after sanding and the sample's surface being exposed. We used oil instead of water to prevent any further alteration at the principal slip surfaces and keep the original composition.

To enhance conductivity and prevent charging during SEM imaging, the exposed slip surfaces of the samples were coated with a thin layer of chromium (Cr) (20nm) using the Quorum Q150T Plus Turbomolecular Pumped Coater, installed at the Department of Geosciences of the University of Padua to provide the precise and uniform coating necessary for high-resolution imaging (Fig 2.8).

Scanning Electron Microscope images were performed with the "TESCAN SOLARIS dual beam FIB-FE-SEM" installed at the Department of Geosciences of the University of Padua. Working conditions for Back-Scattered Electron (BSE) images were 5–7 keV, 300 pA, and 3–4 mm as working distance for the "ultra-high resolution" scan mode, while 15 keV, 3 nA and 3–4 mm as working distance for the "analysis" scan mode. Cathodoluminescence (CL) imaging across the principal slip zones was done under

working conditions of 10 keV, 2 nA, and 16 mm of working distance under the "analysis" scan mode.
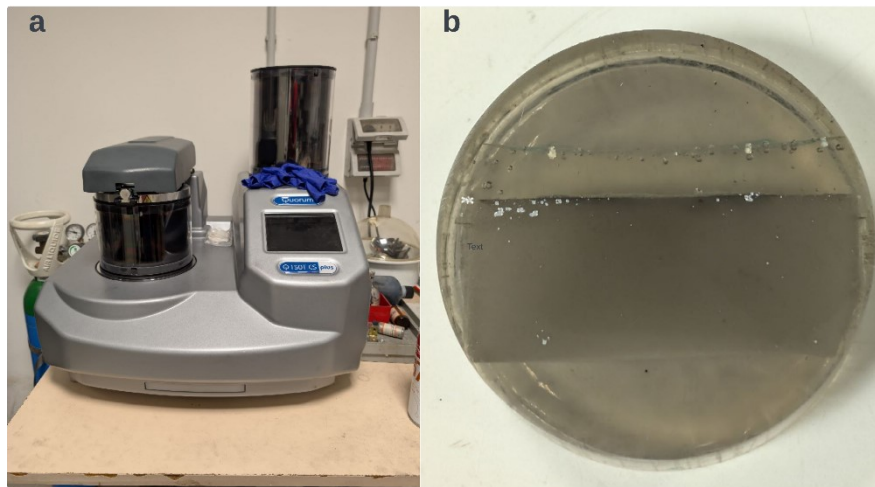

Figure 2.8 a: Turbomolecular Pumped Coater used for the principal slip surface with a thin layer of Chromium (Cr). b: s2016 sample after completing all the preparing steps for SEM analysis.

Chapter 3. Results

Here I describe the (1) mechanical data from experiments s2013, s2016, s2017, and s2019 performed with SHIVA, (2) the micro-Raman, and (3) scanning electron microscope investigations of the experimental slip zones.

3.1. Mechanical data experimental results

All the experiments are performed at constant normal stress (σ_n) of 20 MPa and imposed equivalent slip velocity of 6 $m\ s^{-1}$. In Fig 3.1 is reported the evolution of the shear stress (τ MPa) with slip displacement for experiments s2013, s2016, s2019 (pressurized CO_2), and s2017 (pressurized Ar). The target slip displacement for s2013 was set to 20m and for all other experiments was set to 6m. During the s2013 and s2019 experiments, strong mechanical vibrations due to problems related to the imposed normal stress by the electromagnetic piston occurred from about 4m and 1.8m of slip displacement, respectively. Instead, experiments s2016 and s2017 have no mechanical anomalies from the initiation to the end of slip (6m) (Fig. 3.1). For this reason, first I compare s2016 and s2017 for total slip.
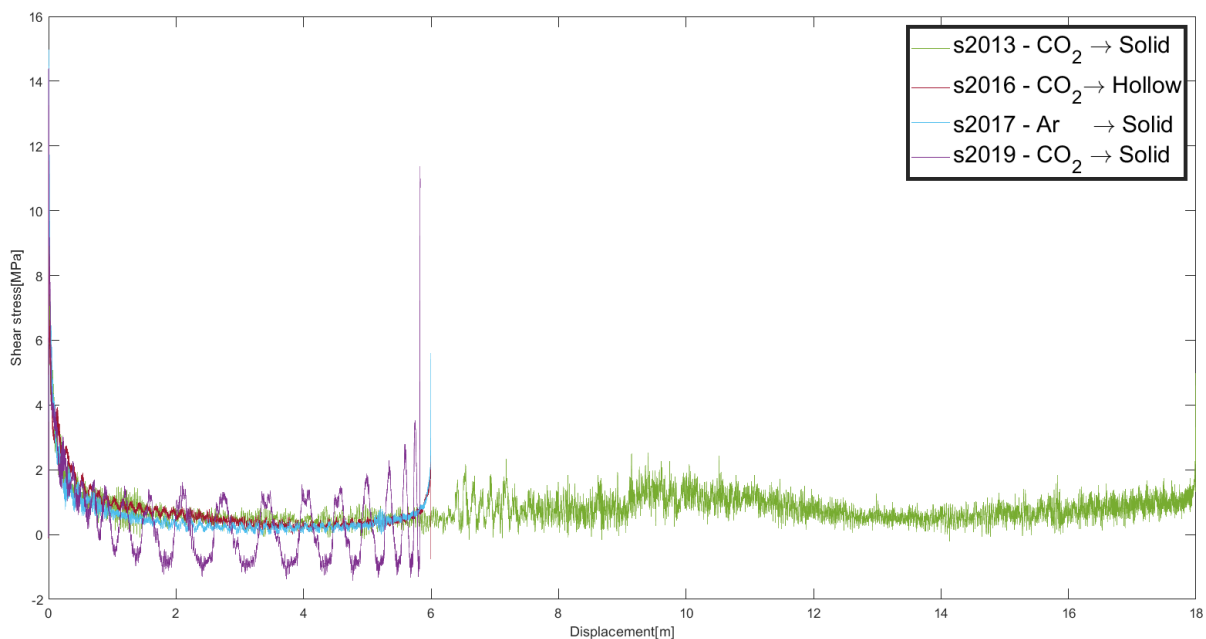

Figure 3.1 Evolution of Shear stress versus displacement of all experiments for whole slip displacement.

Then, to make a reasonable comparison for all experiments I considered the displacement from 0 to 1.8 m to eliminate the effect of mechanical vibration on the outcomes data.

Figures 3.2 and 3.3 report the evolution of the friction coefficient (or measured shear stress divided by normal stress) for experiments s2016 (pressurized CO_2) and s2017 (pressurized Ar), respectively, and of the imposed velocity function with time and slip displacement.

In both experiments, the friction coefficient:

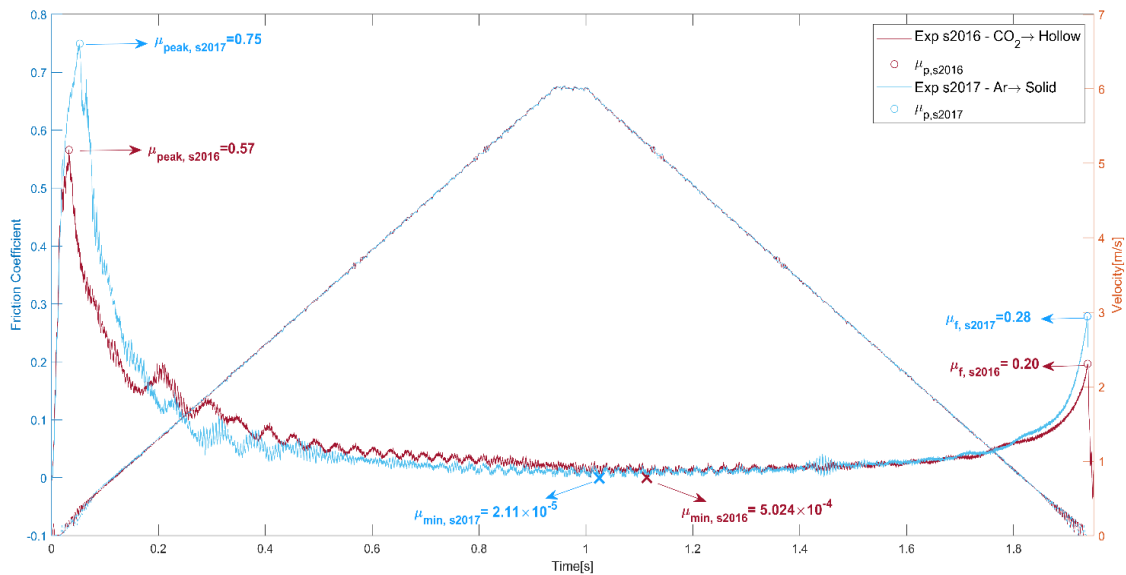1) First increased (i.e., loading stage) at slip initiation to a peak value (μ_{peak})

Figure 3.2 Friction coefficient vs. time for s2016 and s2017 experiments. The experiments lasted 1.95 s. μ_{peak}=peak friction coefficient, μ_f=recovered friction coefficient at the end of each experiment, $\mu_{min}=$ *minimum firction coefficient*

2) Then decreased (i.e., weakening stage), in 300 ms and 1.5-2.0 m of slip, to minimum friction (μ_{min}) and, in general, to a low steady-state value (μ_{ss}) where the value of friction coefficient remains relatively constant and is here determined with the best-fit equation (Nielsen et al. 2016):

$$\tau = (\frac{\tau_p^n}{1 + \left(\frac{u}{u_w}\right)^{\alpha n}} + \tau_{ss}^n)^{1/n}$$

(Equation 3.1)

24

With n=8 (for the details and explanation please refer to the main article).

3) Increased again (i.e., restrengthening stage) at the end of the slip during deceleration (μ_{final}).

In the experiment s2016 performed in pressurized CO_2 has a similar mechanical behavior, with respect to the experiment performed in pressurized Ar although the μ_{peak} is lower (0.57 vs. 0.75), μ_{ss} is higher (0.021 vs. 0.013) and μ_f lower (0.2 vs. 0.28) (Figs 3.2 and 3.3). However, the differences in frictional values could be related to the type of gas used (CO_2 vs. Ar), but also to the different geometry of samples: hollow cylinders for s2016 and solid cylinders for s2017, which may result in a different thermal evolution in the slipping zone (see Chapter 4). In particular, in pressurized CO_2 (Exp. s2016), the peak friction is achieved after 0.0013m of slip (or 32.75ms from slip initiation), at a velocity of $V_p = 0.1988m\ s^{-1}$, while in pressurized Ar (exp. s2017), the peak friction coefficient is achieved after 0.005 m of slip (or 52.90 ms from slip initiation), at a velocity of $V_p = 0.2308\ m\ s^{-1}$(see table 3.1 for details).
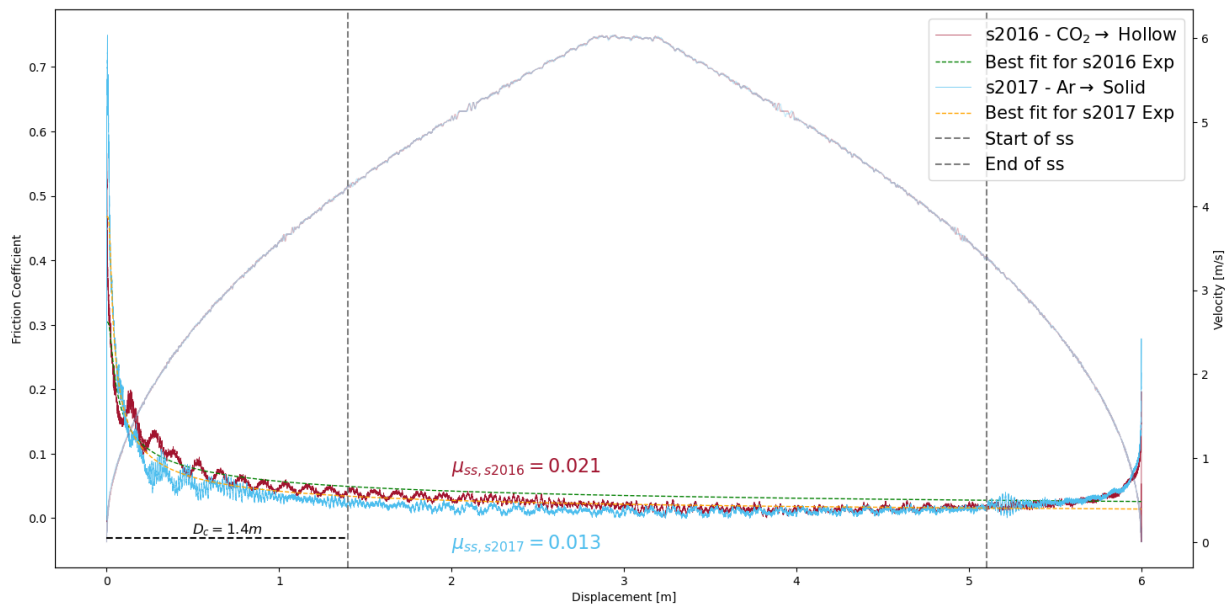

Figure 3.3 Evolution of friction coefficient and velocity with displacement for s2016 and s2019 experiment. Acronyms and symbols: μ_{ss} =steady-state friction coefficient, D_c= The amount of slip displacement, until reaching the steady-state conditions. The μ_{ss} is determined with the best-fit equation (see main text).

Like the steady-state friction coefficient, the μ_{min} is extremely low: 5.024×10^{-4} in pressurized CO_2 and 2.11×10^{-5} in pressurized Ar. These extremely low values may correspond to the spurious friction of the machine.

Fig. 3.4 show the evolution of the friction coefficient and the velocity with slip displacement for all the experiments (s2013, s2016, s2017, and 2019) in the first 0.1m of displacement. The imposed velocity evolution with slip for all experiments was nearly identical except in the very first stage. Here, oscillations in slip velocity during sample acceleration are due to the misalignment of samples which can cause uneven contact surfaces leading to fluctuations in velocity as the samples interact during slip. As stated before, due to its hollow geometry, the s2016 sample experienced a different thermal history than other samples, resulting in a lower peak friction coefficient compared to other CO_2 experiments (see chapter 4).
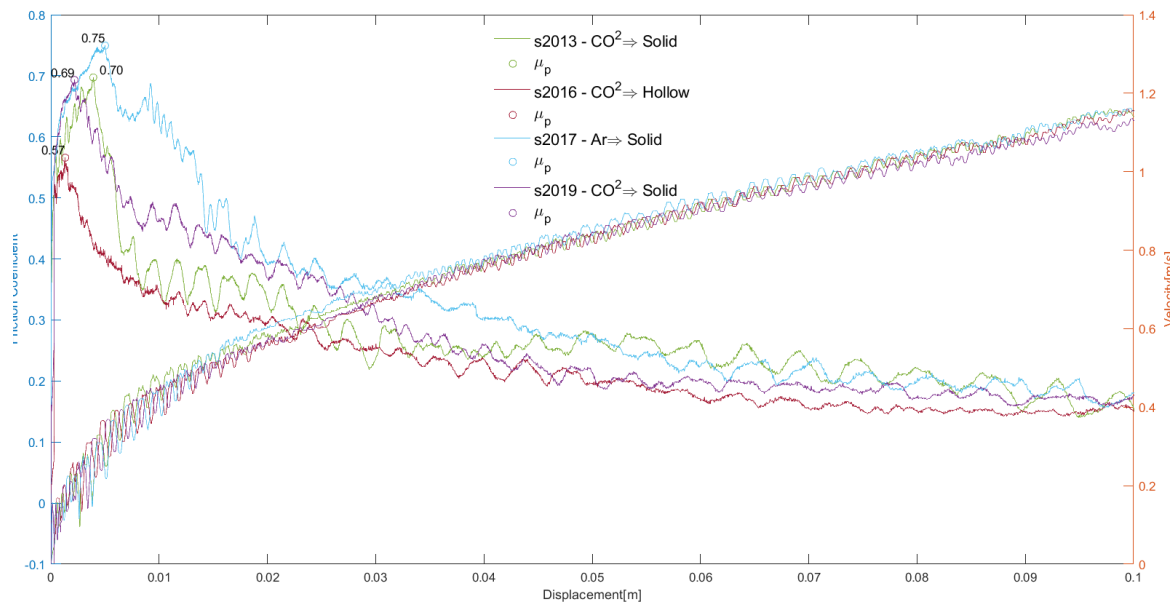

Figure 3.4 Friction coefficient and velocity evolution for all the experiments in the first 10 cm of slip displacement with showing the peak friction coefficient for each experiment. The oscillation of velocity data at slip initiation is probably due to the miss alignment of the samples which caused this kind of vibration in outcomes data.

The similar behavior of the s2013 and s2019 initial friction coefficient evolution in experiments s2013 and s2019 performed both with cylindrical samples and under the same ambient conditions (pressurized CO_2) and loading conditions, demonstrate the

repeatability of the experiments performed with SHIVA also friction machine (see also table3.1).

In presence of pressurized CO_2, experiments s2013 and s2019, the friction coefficient, increased almost linearly (elastic distortion of the machine and sample assemblage) up to $\mu \approx 0.52$, to overcome the static friction coefficient, and then more gradually up to the peak value $\mu_P=0.69$ (Fig 3.5). In the presence of pressurized Ar, s2017, the static friction coefficient is similar (≈ 0.55) but the peak friction is higher, $\mu_{peak} = 0.75$
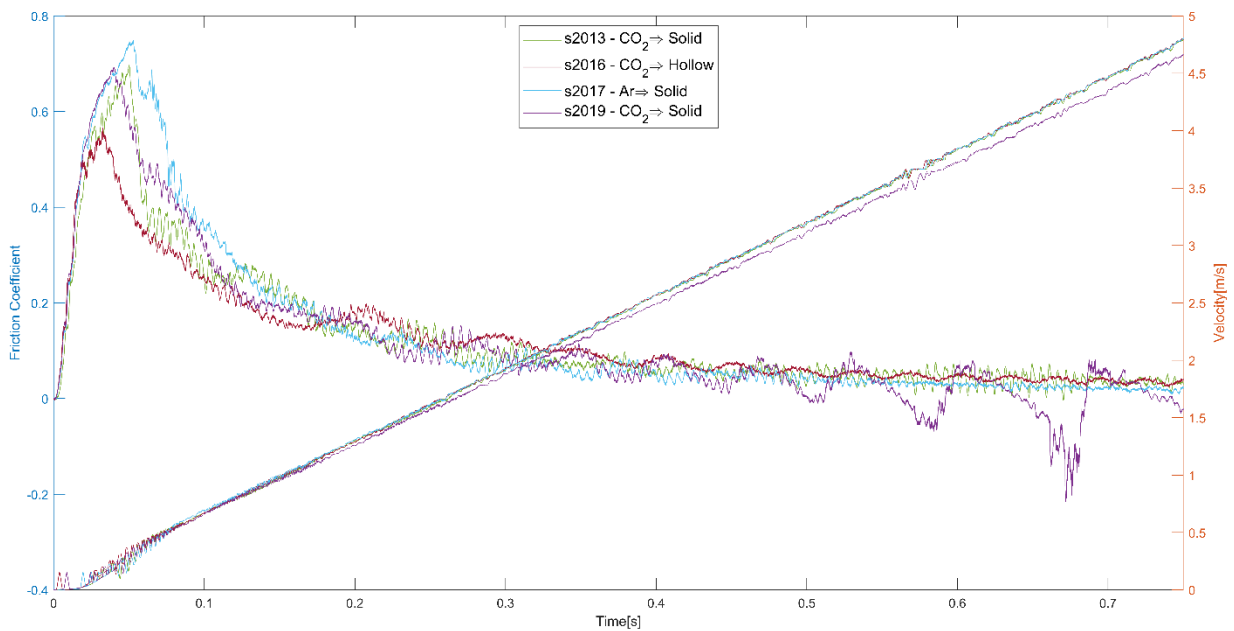

Figure 3.5 Evolution of the friction coefficient and velocity with time from 0 to 750 ms after slip initiation. The time plot shows very identical strengthening for all experiments at first stage.

Fig. 3.5 and 3.6 also show the evolution of friction coefficient and velocity vs. displacement (1.8 m) and time (0.750 s) for all experiments. Roughly after 0.4 m of slip distance (around 0.52s after the slip initiation) all the experiments reached a steady state condition (μ_{ss}).

In the s2016 (pressurized CO_2) and s2017 (pressurized Ar), the samples started to shorten at the initial stage of the experiment (Fig. 3.7). However, in the s2016 experiment (conducted under pressurized CO_2 gas conditions), the sample initiated to dilate just before reaching the steady state condition and continued this dilation up to

the end of the experiment. On the opposite, in the s2017 experiment (conducted under pressurized Ar gas conditions), the sample continued its compaction till reached the steady state condition, remained at this state, and again continued compaction till the end of the experiment(Fig. 3.7).
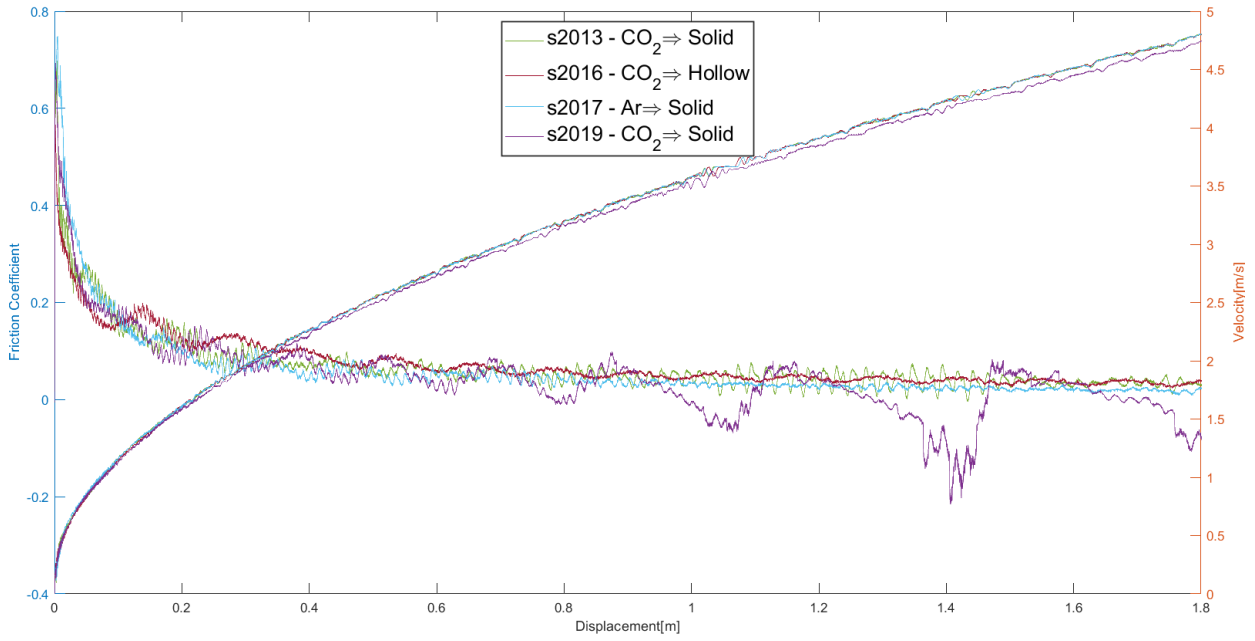

Figure 3.6 Friction coefficient and imposed velocity in the first 1.8 m of displacement for all experiments. The oscillation of the purple plot (s2019) is due to the mechanical instability during the experiments due to the spurious oscillations of the electromagnetic piston of SHIVA which imposes the normal stress (σ_n)
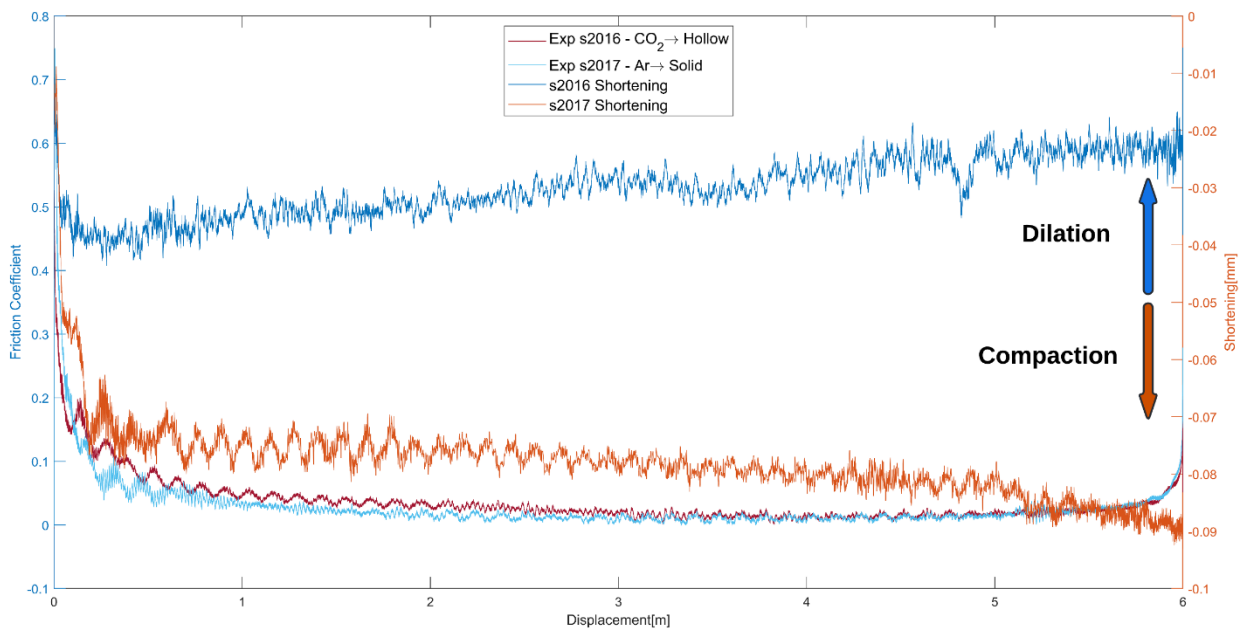

Figure 3.7 Friction coefficient and shortening vs displacement for s2016 and s2017 experiments. Both experiments show an abrupt shortening at the initial stage of experiments.

28

Table 3.1 includes all the mechanical data for all experiments explained in Chapter 3.1.

Exp	s2013	s2016	s2017	s2019
Sample	Solid	Hollow	Solid	Solid
Condition	CO_2	CO_2	Ar	CO_2
τ_M(MPa)	13.86	11.11	14.98	14.40
$\sigma_{n,M}$(MPa)	20.72	21.21	21.24	20.85
μ_p	0.69	0.57	0.75	0.69
μ_{min}		5.024×10^{-4}	2.11×10^{-5}	
μ_{ss}		0.021	0.013	
μ_f		0.20	0.28	
V_p($m\ s^{-1}$)	0.1938	0.1988	0.2308	0.1688
V_{targ}($m\ s^{-1}$)	6	6	6	6
V_{Max}($m\ s^{-1}$)	6.039	6.039	6.039	5.87
δ_p(mm)	3.9	1.3	5	2.2
δ(mm)	17996	5999	5999	5830
t_p(ms)	50.20	32.75	52.90	39.70

Table 3.1 Summary of experimental results. Acronyms and symbols: $\tau_M = Maximum\ Shear\ stress$ (MPa), $\sigma_{n,M} = Maximum\ normal\ stress\ (MPa)$, $\mu_p = Peak\ of\ frictional\ strength(\tau_M/\sigma_{n,M})$, $\mu_{min} = minimum\ Frictional\ strength$, μ_{ss}= steady-state friction coefficient, μ_f= recovered initial friction, V_p= Velocity at peak friction (m/s), V_{targ}= Target velocity($m\ s^{-1}$), $\delta_p = Displacement\ at\ peak\ frioction\ (mm)$, $\delta = Total\ displacement(mm)$, t_p=Time at peak friction(ms).

3.2. Microstructures

In this section, I describe the results of the microstructural analysis performed on the s2016 (pressurized CO_2) and s2017 (pressurized Ar) samples using Scanning Electron Microscopy (SEM) described in chapter 2.3. The analysis highlights the textural and mineralogical variations across different regions of the slip zones. A striking difference between the two samples is the presence, in the polished samples, of a black in color $\ll 100 \; \mu m$ thick layer in the case of the experiment performed in pressurized CO_2, which is absent in the experiment performed in pressurized Ar (compare Fig. 3.8a with Fig. 3.9a).

The post-mortem SEM analysis of the sample s2016 (experiment in pressurized CO_2) reveals a dense network of micro-fractures on both sides of the slip zone. The selected BSE-SEM images (Fig. 3.8b-c-d) highlight the complexity of the microstructure, with numerous micro-cracks propagating through the calcite grains, bordering the about 35 μm-thick slip zone. The latter is made of an ultrafine and continuous aggregate of calcite wrapping rounded 500-800 nm in size C-rich domains interpreted as graphite or amorphous carbon (Fig. 3.8e; elemental analysis performed with EDS, see Ch. 2 - Methods). The presence of C-rich layers is confirmed by micro-Raman analysis (see Chapter 3.3).

The Cathodoluminescence (CL) image offers additional insights into the thermal history of the slip zone (Figure 3.8c). The CL imaging reveals a whitish luminescence in the slip zone and along the grain boundaries in the wall rock. This whitish color is associated with small changes in the composition of calcite, probably due to decarbonation and recrystallization processes during the fault slip ([Han et al. 2007](); [Billi and Toro, 2008]()).

The post-mortem SEM analysis of the sample s2017 (experiment in pressurized Ar), reveals differences compared to the s2016 sample. The slip zone is $a < 15 \; \mu m$-thick slip zone, and with a less extensive fracture network, relatively larger grain size, and a uniform fracturing compared to the slip zone of experiment s2016 (Fig. 3.9a-b).
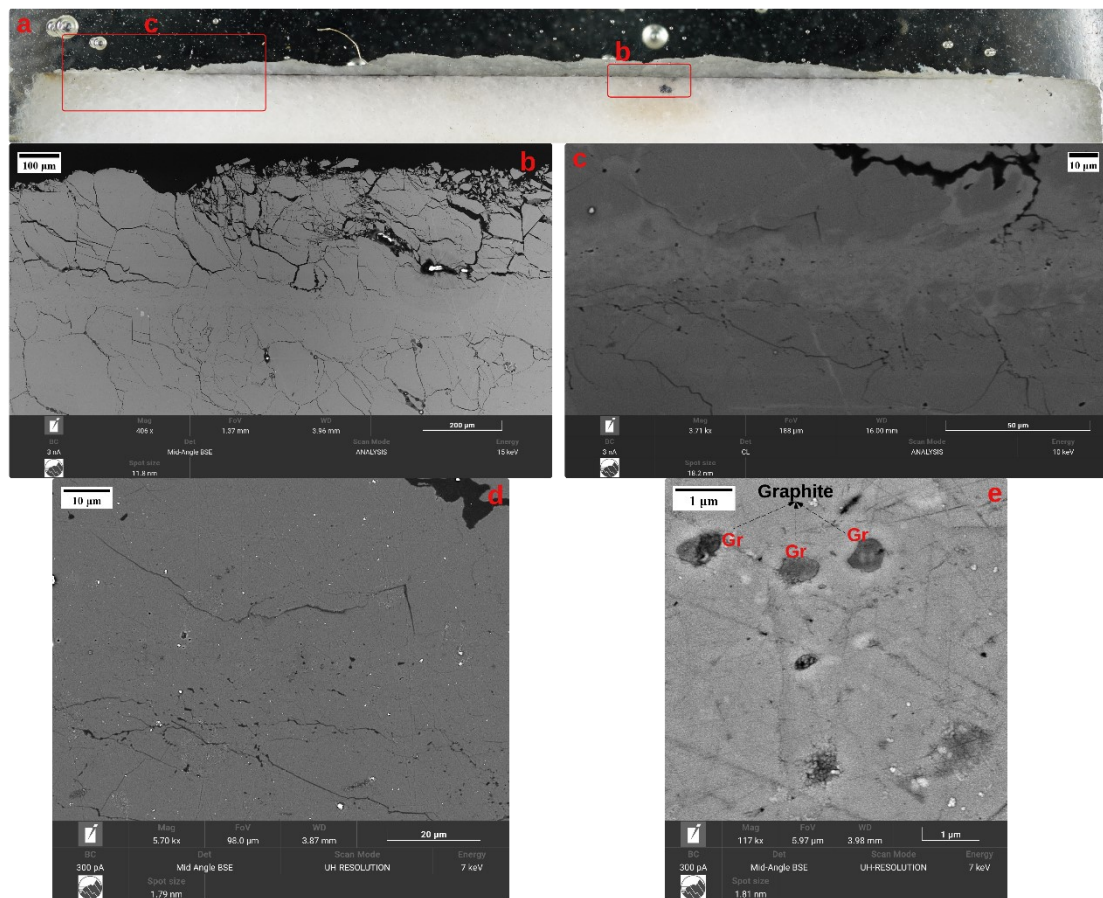
Figure 3.8 Microstructures of the slip zone of experiment s2016 performed under pressurized CO_2. (a) Optical scan of the slip zone, evidence by the continuous black in color layer. (b) Mid-Angle BSE of the slip zone (see box in (a)) showing a network of fractures. (c) Cathodoluminescence (CL) image of region (b). (d) Mid-Angle BSE of the slip zone in (b). (e) High-magnification BSE image of region (c), highlighting pore structures filled with graphite.

The BSE images (Figures 3.9b-c-d-e) at increasing magnifications provide a comprehensive view of the microstructural features. The slip zone is bounded by a damage zone with fewer microfractures compared to the s2016 sample (Fig. 3.10b). The slip zone is locally bounded by a sharp (possibly slip) surface (Fig. 9c) and includes 100-200 nm-in-size grains with straight boundaries (Fig. 9d) possibly due to recrystallization and annealing processes. The slip zone also includes dark in color grains, but their composition has not been determined yet (Fig. 3.9e). The cathodoluminescence image of the slip zone reveals a thinner slip zone and "altered" volume compared to the s2016 sample (Figure 3.9f).
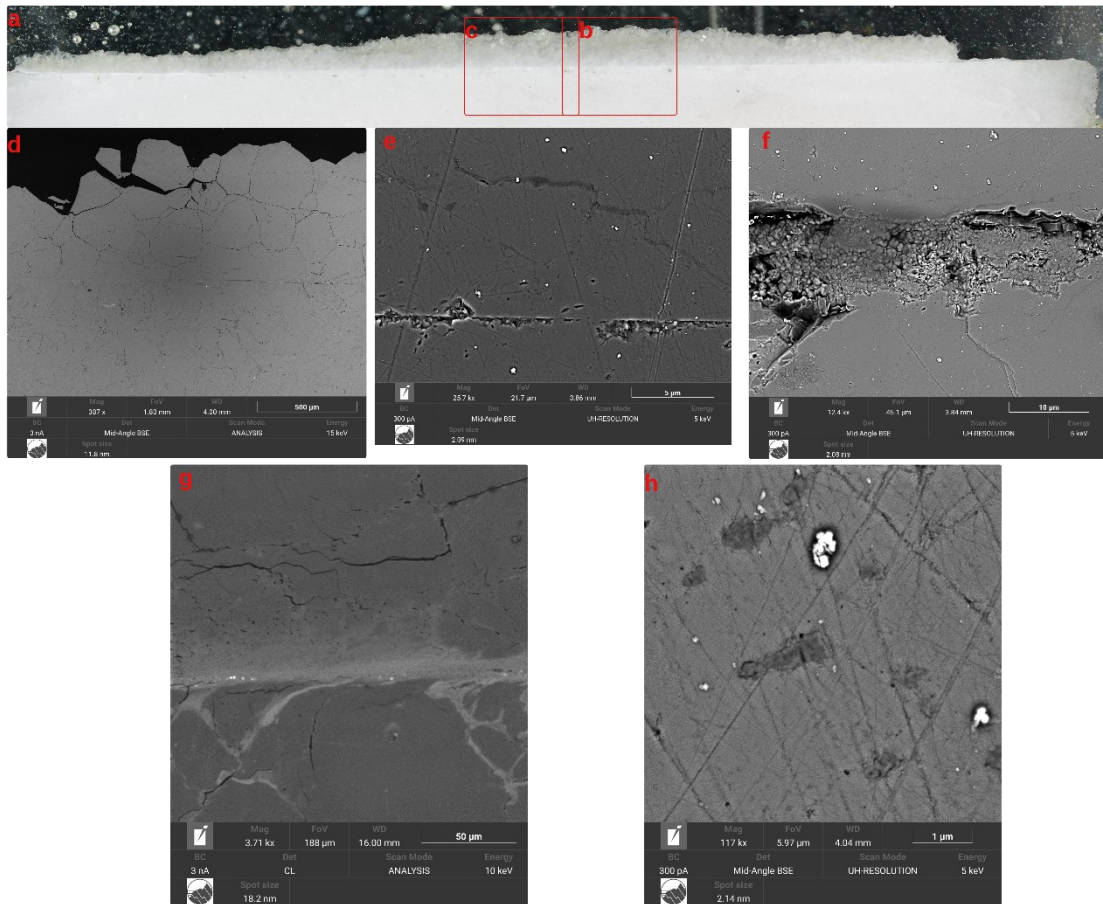
Figure 3.9 Cross-sectional view of the slip zone of s2017sample under high resolution. (a) Overview of the slip zone, highlighting regions of interest (b) and (c). (d) Mid-Angle BSE of the region (b) at 387x magnification, showing the overall structure. (e) High-magnification Mid-Angle BSE of the region (b) at 25.7kx, (f) at 12.4kx, and (h) at 117kx, displaying detailed microstructural features. (g) CL image of region (b), illustrating mineral distributions within the slip zone.

SEM-point spectrum analysis was conducted for the s2017 sample to investigate the elemental composition of dark area in Fig. 3.9h at selected spots. In the brighter regions (Fig 3.10a spectrum 2), calcium (Ca), carbon (C), and oxygen (O) are predominant, indicating the presence of calcite ($CaCO_3$) with small amounts of chromium (Cr) from the coating and traces of magnesium (Mg) (Fig. 10c). In contrast, the darker points exhibit a sharper peak in carbon, which could suggest the presence of small amounts of graphite (Fig. 3.10b-d) (see Chapter 4 for further discussion on graphite presence).
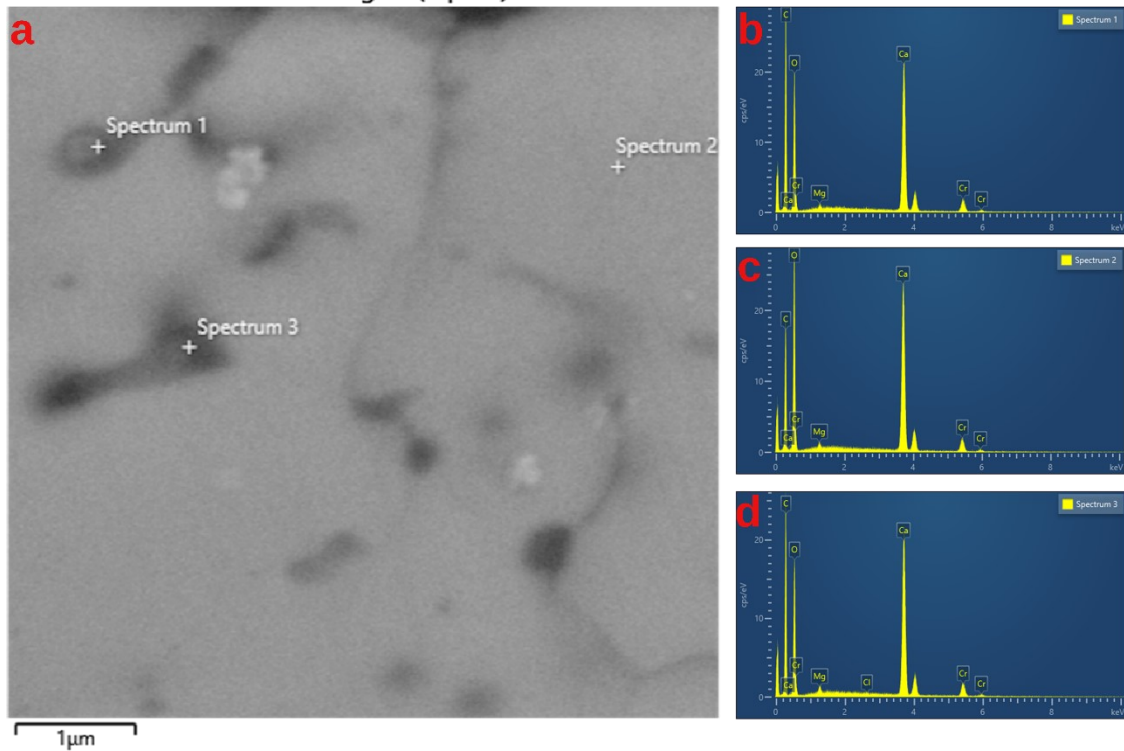
Figure 3.10 SEM-point spectrum mapping of the s2017 sample. (a) SEM image showing selected points for spectrum analysis. (b-d) Spectra from the selected points, showing elemental composition. The bright areas show prominent peaks of calcium (Ca), carbon (C), and oxygen (O), indicating calcite ($CaCO_3$), with small amounts of magnesium (Mg) and chromium (Cr) from the coating. In darker areas, sharper carbon peaks suggest possible graphite content.

3.3. Mineralogy and Geochemistry

I performed SEM-EDS mapping (Energy Dispersive X-ray Spectroscopy) on the slip zone of sample s2016 and micro-Raman spectroscopy on the slip surface of sample s2016.

The SEM-EDS technique provides a detailed visualization of the elemental distribution within the sample by displaying the characteristic X-ray intensities or elemental concentrations across the slip zone (Fig 3.11). Such analysis is essential for gaining insights into the mineralogical and geochemical processes that occurred during the fault slip events. The EDS mapping performed on the s2016 sample provides a detailed two-dimensional display of various elements, superimposed on the backscattered electron (BSE) image.

Backscattered Electron (BSE) Image: The BSE image serves as the reference for interpreting the elemental maps (Figure 3.11). It highlights the high-contrast features within the slip zone, which correspond to variations in atomic number and, by extension, differences in mineral composition.

Magnesium (Mg): The EDS map for Mg shows minor concentrations, primarily manifesting as bright spots along the slip zone.

Calcium (Ca): The calcium map reveals a nearly uniform distribution throughout the sample.
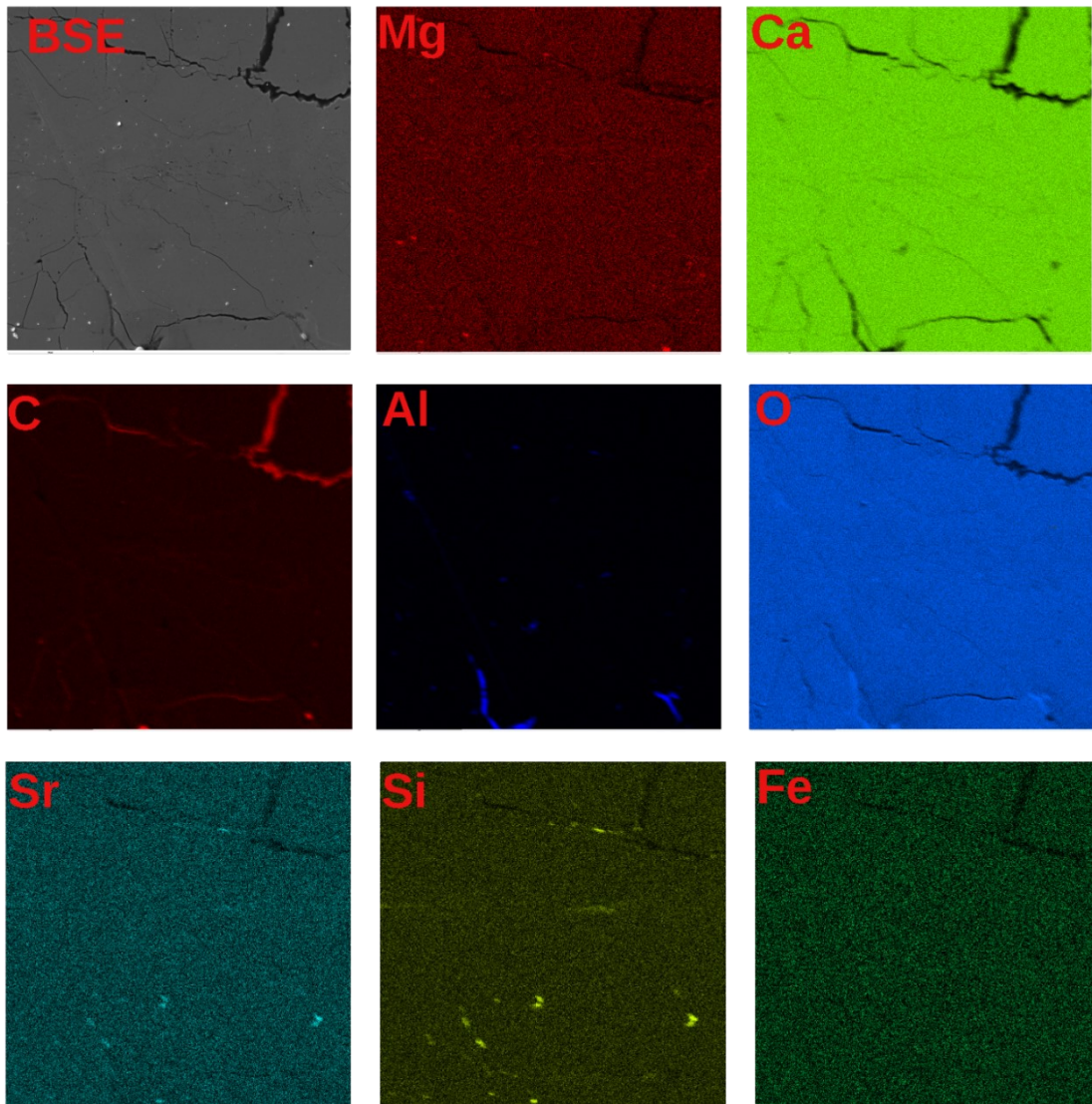

Figure 3.11 Energy Dispersive X-ray Spectroscopy (EDS) mapping of the s2016 sample, illustrating the distribution of key elements across the slip zone. The BSE image (top left) provides a high-resolution structural overview. The EDS maps display the elemental distributions of Magnesium (Mg), Calcium (Ca), Carbon (C), Aluminum (Al), Oxygen (O), Strontium (Sr), Silicon (Si), and Iron (Fe).

Carbon (C): The EDS map for carbon displays bright lines along fracture networks, which are likely due to the presence of embedding resin used during sample preparation. However, considering the possible presence of C as graphite or amorphous carbon, further analysis would be necessary to confirm the origin of these carbon-rich areas.

Aluminum (Al): Aluminum is sparsely distributed across the sample, with minor concentrations detected in the slip zone.

Oxygen (O): The oxygen distribution closely mirrors that of calcium, further supporting the prevalence of calcite within the slip zone.

Strontium (Sr): The Sr map reveals negligible concentrations of strontium, which are concentrated along the slip zone.

Silicon (Si): The EDS map for silicon shows minor concentrations within the slip zone. The presence of Si, although limited, suggests the existence of siliceous impurities or secondary mineral phases, such as quartz or feldspar, within the calcite matrix.

Iron (Fe): The Fe map indicates a negligible presence of iron, suggesting that iron-bearing minerals are not significant components of the slip zone.

The SEM-EDS mapping was also performed on the slip zone of sample s2017. Fig. 3.12 show the distribution of key elements across the slip zone of the s2017 sample.

Backscattered Electron (BSE) Image: The BSE image serves as a reference for understanding the elemental distribution across the slip zone (Figure 3.12). The image reveals areas of contrast, which are associated with differences in atomic number and, consequently, mineral composition.

Magnesium (Mg): The Mg map shows limited concentrations, appearing as minor bright spots scattered along the slip zone. This suggests that magnesium-bearing phases, such as dolomite, are present but in low amounts.

Calcium (Ca): The Ca distribution is almost uniform throughout the sample, indicating that calcite is the dominant mineral phase. This aligns with the observed microstructure, where calcite is the principal constituent.
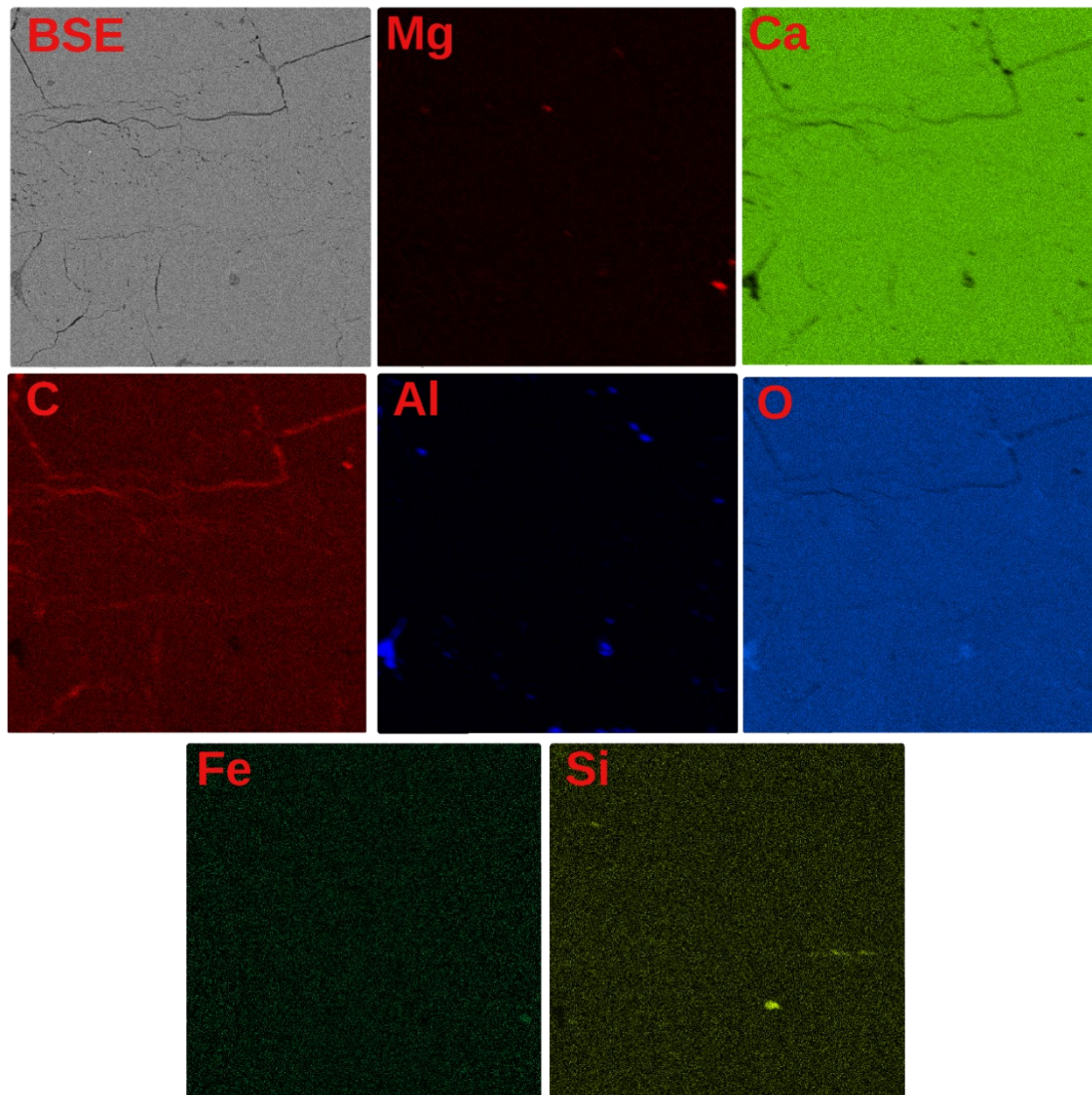
Figure 3.12 Energy Dispersive X-ray Spectroscopy (EDS) mapping of the s2017 sample, illustrating the distribution of key elements across the slip zone. The BSE image (top left) provides a high-resolution structural overview. The EDS maps display the elemental distributions of Magnesium (Mg), Calcium (Ca), Carbon (C), Aluminum (Al), Oxygen (O), Silicon (Si), and Iron (Fe).

Carbon (C): The carbon map reveals linear concentrations along fracture zones. These bright lines may represent embedding resin.

Oxygen (O): The oxygen distribution is largely consistent with the calcium map, supporting the prevalence of calcite ($CaCO_3$) in the slip zone, as oxygen is primarily bonded with calcium to form this mineral.

The EDS maps for Al, Fe, and Si show very negligible concentrations across the sample, which could indicate the presence of trace amounts of other mineral phases containing these elements (Fig. 3.12). Their limited distribution suggests they are not significant

components of the slip zone but may be associated with minor impurities or secondary phases.

Micro-Raman (MR) analysis allows to detection of the vibrational modes of the minerals present, allowing for the identification of stress-induced transformations, phase changes, and the distribution of minerals across the sample. Due to the limited available time, the MR analysis was only performed on the slip surface s2016 sample (Fig 3.13). The banded structure is due to the presence of lineation formed during sliding. The variations in color and intensity across the slip surface suggest heterogeneity in the mineralogical composition, likely caused by thermal decomposition and deformation during the frictional experiment with the SHIVA. In fact, frictional heating can produce high temperatures on the slip surfaces which can lead to the thermal decomposition of calcite during seismic slip into carbon dioxide (CO_2) and calcium oxide (CaO):

$$CaCO_3(s) \rightleftharpoons CaO(s) + CO_2(g)$$
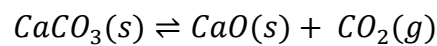
(Equation 3.2)
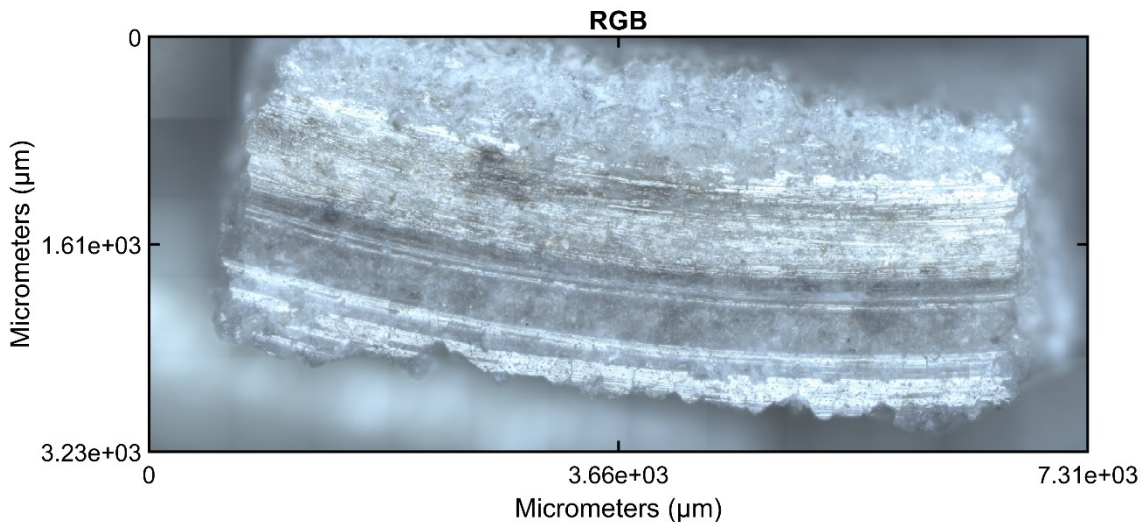
Figure 3.13 Photo of the slip surface of the s2016 experiment (conducted in pressurized CO_2 condition).

The slip surface includes bands consisting of light-gray-in-color and dark-gray-in-color flow structures (Fig. 14). The micro-Raman spectra confirm that the abundant light-gray-in-color domains are mostly composed of calcite (see the prominent peaks in the spectra, particularly around 1086 cm^{-1}, which corresponds to the symmetric stretching

mode of the carbonate ion (CO_3^{2-})). Instead, the less abundant dark-gray-in-color domains include the characteristic G-band around 1580 cm^{-1} and the D-band around 1350 cm^{-1}, which are prominent in the spectrum of graphite (Fig. 15c). The spectrum labeled 'g' shows these peaks more distinctly, whereas the spectrum 'h', although still showing the presence of graphite, is broader and less defined.
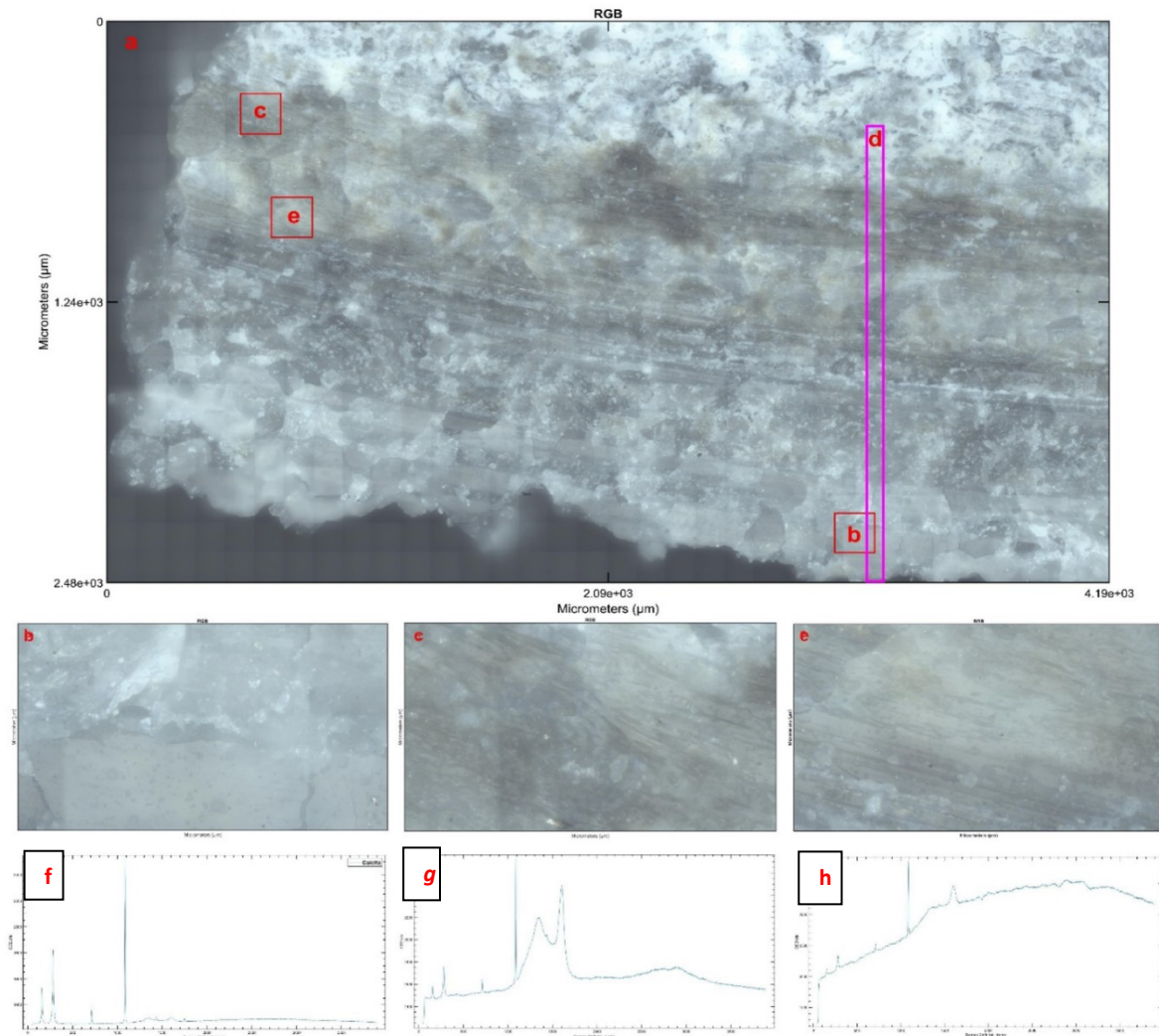
Figure 3.14 Micro-Raman analysis of the principal slip surface from s2016's sample. **a:** shows a high-resolution image of the slip surface with selected zones for detailed analysis. b, c, and e represent magnified views of specific areas on the slip surface. The red long-narrow rectangle, d, outlines the zones subjected to line analysis, shown in Fig13a. Raman spectra from these zones are displayed in panels f, g, and h. Spectrum f is dominated by sharp calcite peaks, while spectra g and h exhibit features indicative of graphite, with spectrum h showing a broader signal, possibly due to mixed carbon phases or structural disorder.

Figure 3.15 presents the detailed line scan of the region 'd' from Figure 3.14, providing an in-depth view of the mineral distribution along the slip surface in a wider area. The

intensity map (Fig 3.15a) highlights regions of high Raman signal intensity, which correspond to areas rich in specific mineral phases.
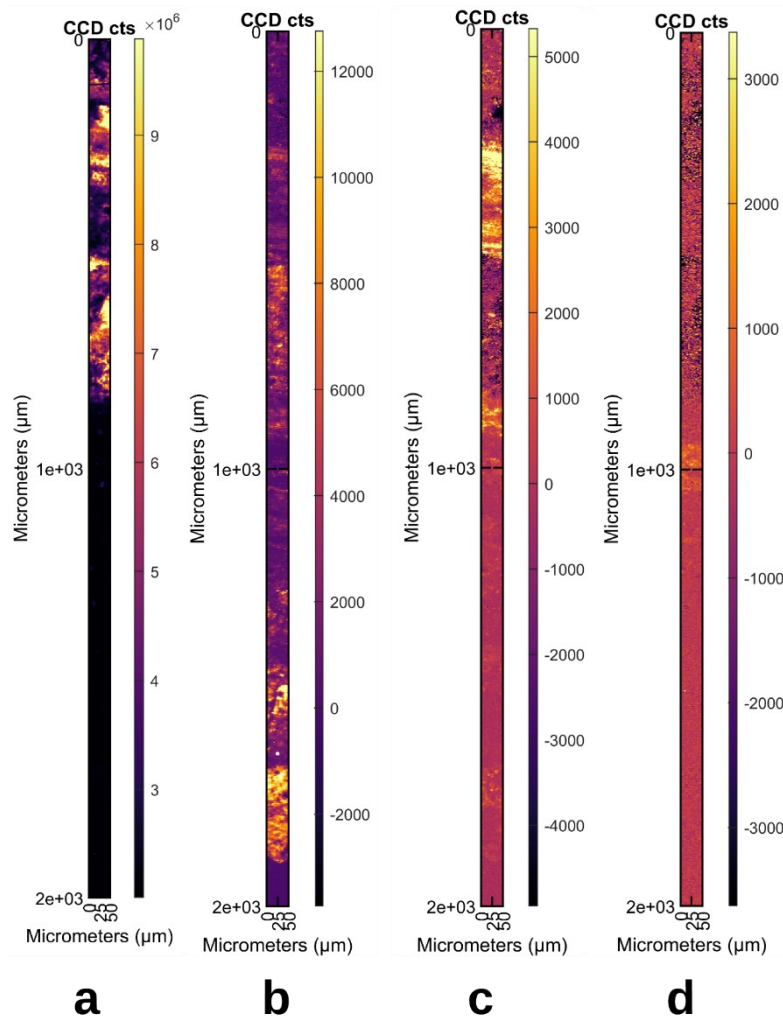

Figure 3.15 Micro-Raman line scan along the principal slip surface of s2016's sample, focusing on the area marked by the red long-narrow rectangle, d, in Figure 3.12. The main scan, a, shows the intensity distribution across the slip surface. Sub-panels, b, c, and d represent intensity maps for specific Raman shifts: **b:** corresponds to calcite (1000–1100 cm^{-1}), c represents graphite (1500–1700 cm^{-1}), and (d) depicts an unidentified peak (3350–3700 cm^{-1}). The distribution of these mineral phases highlights the complex chemical interactions and material transformations occurring along the fault during seismic events.

Figure 3.15b focuses on the Raman shift between 1000 and 1100 cm^{-1}, corresponding to the calcite region in Fig 3.14d. The intensity in this range is consistent across the scanned area, confirming the widespread presence of calcite along the slip surface. The distribution of graphite is less uniform than that of calcite, with certain areas showing higher intensities (Fig3.15c). The peak observed in the range of the intensity between

3500 and 3700 cm^{-1} is less common and suggests the presence of an unusual mineral phase (Fig. 3.15d).

Chapter 4. Discussion

The main goal of the thesis, compared to the hundreds of experiments reproducing seismic slip conditions with Carrara marble but under room-humidity (Han et al., 2007; 2010; Spagnuolo et al., 2015) or pressurized water conditions (Violay et al., 2014; 2015), was to investigate for the first time the role of pressurized CO_2 during seismic faulting. This condition might occur also in fault patches in earthquakes hosted in carbonate-rich rocks (e.g., Miller et al., 2004).

Here I briefly discuss the similarities and differences between the mechanical behavior of experimental faults made of Carrara Marble (99% calcite) in the presence of pressurized CO_2 and Ar. In fact, since the rock type and the loading conditions were the same, the differences in the mechanical behavior could be related to:

1) sample shape: s2013, s2017 and s2019 were performed with solid cylinders; s2016 with hollow cylinders;

2) environmental conditions: experiments s2013, s2016 and s2019 were performed with pressurized CO_2; s2017 with pressurized Ar.

I wish to highlight that the results I presented in the thesis (5 months of work in total) are preliminary and further experiments and micro-analysis are required to understand better the processes activated during simulated seismic slip in carbonate-rich rocks. Moreover, only in experiments s2016 and s2017 I could recover the specimens after the test. In fact, the spurious oscillations of the axial electromagnetic piston in experiments s2013 and s2019 resulted in sample failure (Fig. 3.1).

4.1. Mechanical behavior

4.1.1 Friction at slip initiation

The frictional evolution of s2016 (pressurized CO_2), and s2017 (pressurized Ar), show different mechanical behavior ($\mu_{p,s2016} = 0.57$ vs $\mu_{p,s2017} = 0.75$ and $\mu_{ss,s2016} =$

$0.021 \ vs \ \mu_{ss,s2017} = 0.013$) (Fig. 3.2). Since the loading conditions are identical (same normal stress, same acceleration, etc.), these differences could be either due to the type of the gas we used during each experiment or difference in sample shape: hollow cylinders for s2016 and solid cylinders for s2017 (Fig. 2.3), which may result in a different thermal evolution in the slipping zone. In fact, temperature evolution in the slipping zone has a pivotal role in the frictional evolution of the sliding interface (Nielsen et al., 2021; Aretusini et al., 2021).

The slip rate (or sliding velocity) is a function of angular velocity ($\omega \ in \ rad \ s^{-1}$) and the radius of the sample (r):

$$V = \omega r$$

(Equation 4.1)

Also, the temperature in the sliding surface increases with slip rate and shear stress (or friction) with time t of sliding (Di Toro et al., 2006):

$$\Delta T \propto V_{slip}.\tau.\sqrt{t}$$

(Equation 4.2)

The two above equations demonstrate a clear distinction in thermal evolution in the slip surfaces between solid and hollow cylindrical samples (Fialko and Khazan. 2006). In fact, at slip initiation, from Eq. 4.1, in the case of solid cylinders, the sliding velocity is nominally zero (r = 0) at the sample center, while is large at the edge of the sample. As a consequence, the temperature increases abruptly at the sample edge (Eq. 4.2) but slowly at the sample center. Here, the temperature increase is also controlled by heat diffusion from the sample edge towards the core, which is slow in rocks because of their thermal conductivity. Since frictional weakening in carbonate rocks is mostly controlled by the activation of temperature-dependent deformation processes (Spagnuolo et al., 2015; De Paola et al., 2015; Nielsen et al., 2021), hollow cylinders weaken earlier than solid cylinders (Fig. 3.4). However, after ~1 s of slip, this different initial temperature evolution disappears and the frictional strength is similar in both experiments (see Fig. 3.2).

Instead, the comparison of the frictional evolution with slip displacement at slip initiation (Fig. 3.4) in experiments performed with cylindrical samples in the presence of pressurized Ar (s2017) or pressurized CO_2 (s2013 and s2019) shows that friction is higher in the presence of Ar. First, the fact that the two experiments s2013 and s2019 performed under pressurized CO_2 exhibited very similar mechanical behavior (peak friction coefficient, friction decay, etc.: Fig. 3.4) highlights the repeatability of the experiments performed with the SHIVA machine allowing me to discuss the observed mechanical differences with respect to the experiment s2017 (Ar). In particular, the faster decrease of friction coefficient observed in experiments s2013 and s2019 performed under pressurized CO_2, may be attributed to the more abundant formation of amorphous carbon and graphite along the slip zone in experiment s2013 (Spagnuolo et al., 2015).

During high-velocity friction calcite in the slip zone can be transformed into graphite (Gr) by mechanically and thermally driven graphitization (Chen et al., 2023; Kuo et al. 2014; 2017; Oohashi et al., 2011).

Oohashi et al. (2011) state that, with increasing temperature, two possible reaction pathways lead to the formation of graphite:

$$CaCO_3(s) + 4H_2 \rightarrow CaO(s) + CH_4(g)$$
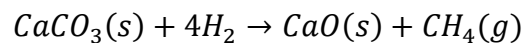
(Equation 4.3)

and the subsequent pyrolytic dissociation of CH_4:

$$CH_4(g) \rightarrow C(s) + 2H_2(g)$$
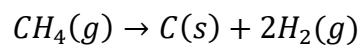
(Equation 4.4)

Another possible reaction pathway, which does not require CH_4, and it is more likely to occur under our experimental conditions is (commonly at T > 800°C, though it may occur also at lower bulk temperatures in the slipping zone: Spagnuolo et al., 2015; Aretusini et al., 2021):

$$CaCO_3(s) \rightarrow CaO(s) + CO_2(g)$$
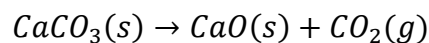
(Equation 4.5)

Following the reduction reaction of CO_2:

$$CO_2(g) + 2H_2(g) \rightarrow C(s) + 2H_2O(g)$$

(Equation 4.6)

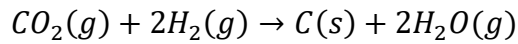The micro-Raman spectrum shows a peak at 3600cm^{-1} which is typically associated with the O-H stretching mode in water (Avila et al. 1999) (Fig 4.1). This hydroxyl group (OH$^-$) or water vapor (H_2O (g)), could generated from (1) the presence of moisture which was not entirely eliminated during sample preparation or handling, and (2) the above-mentioned reactions during the formation of graphite (Gr) in the slip zone. The graphite can act as a solid lubricant leading to reducing the frictional strength of fault. Since, at the initiation of slip, there is more CO_2 in experiments s2013 and s2019 than in experiment s2017 performed in Ar, we may expect that reaction 4.6 is more efficient at slip initiation in the presence of pressurized CO_2 and Gr is produced earlier or is more abundant. As a consequence, the experimental fault of Carrara marble in pressurized CO_2 is weaker and the friction coefficient decays earlier than in the experiment performed in pressurized Ar (see Fig. 3.4).
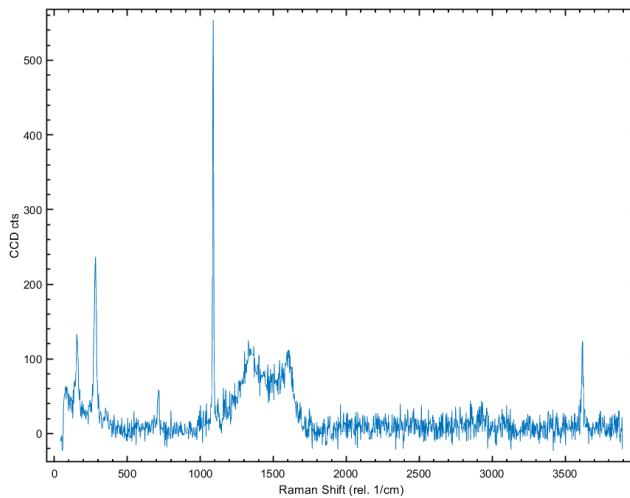
Figure 4.1 *Raman spectrum from s2016 experiment (pressurized CO_2 showing peaks related to calcite, Graphite and water).*

4.1.2 Friction at steady-state

While at slip initiation there are differences in the evolution of the friction coefficient depending on the type of pressurized gas, once the steady-state conditions are achieved, the frictional strength is very similar for all the experiments (Figures 3.3 and 3.5). As previously observed for experiments performed under room humidity conditions, friction at steady-state is negligible, and approaches μ ≈ 0 (Violay et al., 2014;

2015). Such extremely low values of friction coefficient have been attributed to the formation of nanoparticles in the slip zone, due to fragmentation and decarbonation of calcite grains, which activate grain-size and temperature-dependent processes ("grain diffusion-controlled" superplastic behavior: Spagnuolo et al., 2015; De Paola et al., 2015; Pozzi et al., 2021; Demurtas et al., 2019; Nielsen et al., 2021; Cornelio et al., 2022). Moreover, sub-micron in size patches of amorphous carbon was detected on the slip surface after experiments performed at room humidity conditions (Spagnuolo et al., 2015).

In the experiments presented here, the production of Graphite is larger in the experiments performed in pressurized CO_2 than in Ar, as is possible to appreciate by the presence of a black-in-color layer decorating the slip surface and the slip zone in experiments s2013, 2016, and s2019 at the end of slip (Figures 2.6 and 2.7). This dark layer is not observed in the experiment s2017 performed in pressurized Ar (Figures 2.6 and 2.7). Micro-Raman analysis and the observations with reflected light of the lineated slip surface, show that this dark layer is largely composed of graphite organized in "flow structures" (Fig. 3.13). This structural arrangement suggests that graphite formed during the slip and possibly also during the cooling of the slip zone at the end of the slip. But other than this striking difference in color under the optical microscope, the high-resolution imaging and analysis of the recovered slip zones (FESEM-mid-angle and Cathodoluminescence images, EDS maps) do not show relevant differences. Actually, the slip zones, independently if recovered after the experiment performed under pressurized CO_2 (s2016) or pressurized Ar (s2017) are almost identical. In particular, the slip zones have:

1) uniform gray color in BSE-SEM images (compare Fig 3.8b, pressurized CO_2, with Fig. 3.9d, pressurized Ar) corresponding to the dominant presence of calcite. This suggests that calcite (or a Ca-bearing mineral like CaO produced by decarbonation during sliding but that reacted with CO_2 at the end of the slip to produce $CaCO_3$ – see also point 2 below) had a crucial role in accommodating deformation along the fault slip;

2) light gray color in CL images (compare Fig. 3.8c, pressurized CO_2, with Fig. 3.9g, pressurized Ar), with haloes decorating micro-cracks and grain boundaries, possibly resulting from calcite decarbonation, also along fractures where the hot CO_2 is migrating from the slipping zone, and re-crystallization with the newly formed grains of calcite having slightly different chemical composition (possibly changes of the order of tens of ppm of Fe or Mg or other elements) with respect to the original calcite;

3) identical elemental distributions from EDS maps (compare Fig. 3.11, pressurized CO_2, with Fig. 3.12, pressurized Ar). The uniformity of Ca distribution is accompanied by a similar pattern for O and C, which is consistent with the abundance of calcite in the slip zone. Mg, Al, Si, and Fe have negligible concentrations across both samples s2016 and s2017. The occurrence of these elements is consistent with the presence of accessory minerals, such as dolomite (e.g., Mg), white mica, feldspar and quartz (e.g., Si), and iron oxides (e.g., Fe) which might have breakdown during fault slip;

4) uniform calcite-rich matrix wrapping particles of graphite/amorphous carbon (compare Fig. 3.8e, pressurized CO_2, with Fig. 3.9h, pressurized Ar). These particles could be interpreted also as graphite/amorphous carbon-filled pores (according to this interpretation, the pores are filled by Carbon during cooling after the slip event where temperatures are up to 1200°C, Aretusini et al., 2021).

The whitish-color layer observed in the CL-images is found in the slip zone and in the nearby microfractures and is the result of decarbonation and re-precipitation of calcite (Eq. 4.5). As a consequence, at steady-state, when the friction coefficient is $\mu \approx 0$, the deformation process that controls the fault strength at seismic slip is the same, independently of the presence of pressurized CO_2 or Ar (and room-humidity for the experiments performed in the past, e.g., Violay et al., 2014). The most probable deformation process active at this stage is grain size and temperature-dependent (e.g., super-plasticity driven by grain boundary diffusion, De Paola et al., 2015). At this stage, temperatures in the slipping zone can be as large as 1200°C (Aretusini et al., 2021). Instead, the contribution to the bulk fault weakening of the formation of graphite or amorphous carbon is probably negligible at steady-state conditions. In fact, though

graphite may act as a solid lubricant in fault zones, reducing the overall friction and facilitating slip ([Ooashi et al., 2014](#)), and formed mainly on the slip surface of the experiment conducted with pressurized CO_2 (Figures 2.6, 2.7 and 3.13) the microstructures and the steady-state friction coefficient are identical to those of the experiment performed in pressurized Ar. None of the microstructures found in the slip zones produced in these experiments can be related to frictional melting and rapid quenching of calcite (e.g., the presence of microlites that could be associated with the formation "carbonate-built pseudotachylytes").

4.2. Implications for Fault Mechanics

The goal of the thesis was to highlight the role of environmental conditions in controlling seismic slip in carbonate rocks and to investigate the deformation processes activate during seismic faulting. the experiments were performed under the hypothesis that a CO_2 atmosphere could enhance calcite melting (see Chapter 1.3) and explain the evidence of calcite melting in confined experiments (e.g., [Passelègue et al, 2019](#)). However, in our experiments, we have no clear evidence of calcite melting even under CO_2 conditions. I observed small differences in mechanical behavior at slip initiation, depending on the presence of pressurized CO_2 or pressurized Ar (Figures 3.2 and 3.5). In general, the evolution of the friction coefficient with slip is very similar to the one observed in room-humidity, vacuum, and water-pressurized experiments in Carrara marble under identical loading conditions ([Violay et al., 2014](#)) (Fig. 4.2a).

In the experiments performed under vacuum (s614), the friction coefficient at slip initiation is generally higher and decays towards steady-state conditions more slowly than under room humidity conditions ([Violay et al., 2014](#)) (Fig. 4.2b). This behavior is similar to the one of experiment s2017 under Ar conditions, an inert gas, compared to the one under CO_2 conditions (Fig. 3.4). These observations suggest that is the presence of H_2O or CO_2 that renders fault strength lower at slip initiation (Fig. 3.4 and 4.2). However, these initial differences in frictional strength are very small and disappear once some slip displacement (> 0.5 m) is accommodated by the experimental fault. With increasing slip, the friction coefficient becomes very small independent of the

environmental conditions (CO_2, H_2O, vacuum, Ar). Fault strength at seismic slip rates in carbonate rocks is extremely low and it is eventually controlled by other fault parameters, especially fault roughness and fault complexity.
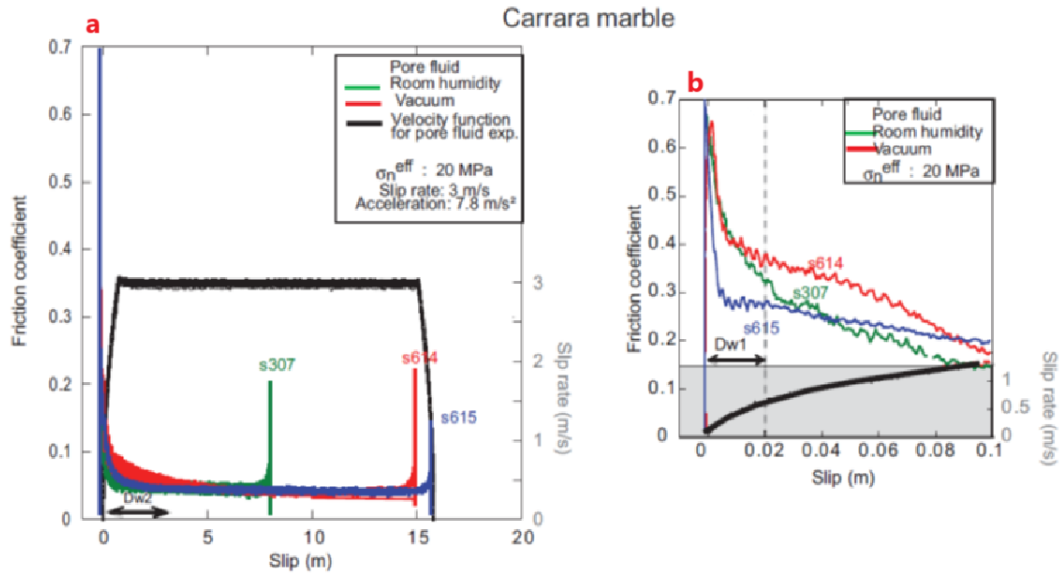
Figure 4.2 Friction coefficient evolution of experimental faults of Carrara marble in the presence of room humidity (green curve), pressurized water (blue curve) and vacuum (10^{-4} mbar, red curve) from Violay et al., 2014. The imposed slip rate was V = 3 m s^{-1} (black curve), acceleration = 7.8 m s^{-2} and σ_n^{eff} (effective normal stress) = σ_n − σ_f = 20 MPa (with P_f = pore fluid pressure = 5 MPa). (a) Friction evolution with slip displacement (entire experiment, up to 15 m of slip). (b) Friction coefficient at slip initiation (first 10 cm of slip).

Chapter 5. Conclusion and Future Works

The primary aim of this thesis, unlike previous studies that used Carrara marble in room humidity, vacuum, or water-saturated environments (Violay et al., 2014), was to examine the impact of pressurized CO_2 during seismic faulting, a condition that may also exist in certain earthquake zones. The experiments conducted using the SHIVA apparatus on Carrara marble samples provided significant insights into the deformation processes and the role of environmental conditions in fault dynamics.

5.1. Main conclusions

The key findings of this study are as follows:

5.1.1 Mechanical Behavior of Faults Under CO₂ and Ar Conditions

The frictional behavior of carbonate faults exhibited slightly different responses to the type of pressurized gas present during simulated seismic slip (imposed slip rate 3 m/s) (Figures 3.1, 3.2, and 3.4). Experiments conducted in the presence of pressurized CO_2, resulted in la ower peak friction coefficient and faster friction decay towards steady-state friction compared to those performed under pressurized Ar (Fig. 3.5). This observation suggests that the presence of CO_2 may facilitate fault slip initiation, promoting the formation of lubricating phases like graphite or by inducing other physical and chemical changes within the fault slip zone. Despite the initial differences in frictional evolution, both environments (pressurized CO_2 or Ar) ultimately resulted in similar steady-state friction coefficient close to zero (Fig. 3.3). This mechanical convergence implies that the environmental conditions (this thesis: pressurized CO_2 or Ar; Violay et al., 2014: room humidity, vacuum or pressurized H_2O) matter only at slip initiation and their contribution to seismic fault weakening is negligible once the friction coefficient evolves towards a minimum or steady-state conditions (Figures 3.4 and 4.2). Instead, the very low friction coefficient (or the coseismic fault strength) is the result of temperature- and grain-size-dependent processes. In this stage of seismic fault slip, the

temperature increases due to frictional heating causing calcite breakdown, resulting in CO_2 release, grain fragmentation (which is in addition to that due to abrasive frictional wear), and nanoparticle formation. At this stage, the fault slip zone is a sort of closed system and the "external" environmental conditions (presence of H_2O, CO_2, Ar, etc.) are irrelevant for the frictional evolution during seismic slip.

5.1.2 Microstructural and Mineralogical Changes

The most striking microstructural difference between the experiments performed in the presence of pressurized CO_2 (s2013, s2016, and s2019) with respect to the experiment performed in pressurized Ar (s2017) is the presence of a < 0.3 mm thick but visible continuous black in color layer decorating the slip zone (Figures 2.6 and 2.7). Curiously, detailed SEM, SEM-cathodoluminescence, and EDS analyses did not reveal relevant microstructural differences within the slip zones of the CO_2 and Ar experiments (compare Figure 3.8 with Fig. 3.9 or Figure 3.10 with 3.11). Both slip zones, less than 0.1 mm-thick (the slip zone from experiment s2016 (CO_2) is slightly thicker), include ~ 1 μm in size particles of graphite wrapped by a continuous matrix made of sub-micron in size calcite grains (Fig. 3.8e and 3.9h). Instead, the micro-Raman investigation revealed the abundant presence of graphite/amorphous carbon on the slip surface of experiment s2016 performed in pressurized CO_2 (Figures 3.13 and 3.14). The identification of graphite is noteworthy as it may act as a solid lubricant especially at slip initiation, contributing to lower the fault frictional strength in the experiments performed under pressurized CO_2 (Fig. 3.4). However, most of the graphite/amorphous carbon probably precipitated in a reduced environment (pressurized CO_2) during the late stages of seismic slip (see the flow structures in Fig. 3.13e-f) and during cooling after the slip event. This interpretation would be in agreement with the absence of a continuous graphite layer in the slip surface of the experiment performed in the presence of pressurized Ar (s2017). In the latter case, graphite is found only locally in the slip zone (Fig. 3.9h) possibly because only here reduced conditions were achieved due to the continuous release of CO_2 from decarbonation of calcite (see also Spagnuolo et al., 2015). These microanalytical observations highlight the critical role of external

environmental conditions in influencing mineralogical transformations, though the resulting mechanical behavior of faults during seismic slip might be similar as discussed above (see Figures 3.4 and 4.2).

5.1.3 Role of Calcite and Other Mineral Phases in Frictional Strength Reduction

Micro-Raman spectroscopy, SEM, and EDS mapping confirmed the predominance of calcite within the slip zones (Figures from 3.8 to 3.14). The ductile behavior of calcite under elevated temperatures likely played a crucial role in accommodating deformation and contributing to the observed low steady-state friction in both CO_2 and Ar experiments. The possible deformation mechanism is temperature- and grain-size-dependent (see Spagnuolo et al., 2015; De Paola et al., 2015; Pozzi et al., 2021; Demurtas et al., 2019). While trace amounts of other elements like Mg, Si, and Al suggested the breakdown of secondary mineral phases (dolomite, mica, etc.), their influence on the overall fault behavior appeared to be limited. This further emphasizes the primary role of calcite in governing fault mechanics during seismic slip.

5.1.4 Repeatability and Reliability of Experimental Observations

The consistency in mechanical behavior between experiments s2013 and s2019, which mirrored the responses of s2016 and s2017, respectively, highlights the repeatability and reliability of the SHIVA experimental setup in simulating seismic slip. This reproducibility is essential for validating the experimental approach and ensuring that the observed phenomena are not isolated occurrences but rather represent fundamental aspects of fault mechanics under varying environmental conditions.

5.2. Implications and Future Work

The findings from this thesis have several implications for understanding fault mechanics in carbonate-rich seismic zones. The influence of CO_2 on reducing fault friction and facilitating slip highlights the potential for CO_2-rich environments to alter

fault behavior, potentially impacting earthquake dynamics in natural settings. The presence of graphite within the slip zone, promoted by the reduced. environment associated with pressurized CO₂, points to the importance of chemical and mineralogical changes in modulating fault strength and slip behavior especially at slip initiation.

Future work should focus on first performing other experiments in the presence of pressurized Ar to confirm the trend observed in Figure 3.4. Then, other experiments should be performed in the presence of pressurized CO_2 but stopped after a few cm of slip to further characterizing the role of CO₂ in facilitating graphite formation and its impact on fault lubrication at slip initiation. Additional experiments with varying CO₂ pressures and temperatures could provide more insight into the conditions that favor graphitization. Moreover, advanced microstructural and geochemical analyses, such as transmission electron microscopy (TEM) and isotope studies, could elucidate the mechanisms behind the observed mineralogical transformations and their implications for fault slip.

In conclusion, this thesis contributes to the understanding of fault dynamics in carbonate-built faults. In particular, environmental conditions (this thesis: pressurized CO_2 or Ar; Violay et al., 2014: room humidity, vacuum or pressurized H_2O) contribute significantly to the evolution of fault frictional strength at the beginning of seismic slip. However, once seismic slip increases, the environmental conditions have a limited role in controlling fault friction. Instead, environmental conditions contribute to the particular mineral assemblage or amorphous phases that form during cooling after the slip event. These insights not only enhance our understanding of fault mechanics but also have broader implications for assessing the potential impact of CO₂-rich environments on seismic activity.

References

1. Aretusini, S., Núñez-Cascajero, A., Spagnuolo, E., Tapetado, A., Vázquez, C., & Di Toro, G. (2021). Fast and Localized Temperature Measurements During Simulated Earthquakes in Carbonate Rocks. *Geophysical Research Letters*, *48*(9), e2020GL091856. https://doi.org/10.1029/2020GL091856

2. Ashby, M. F., & Verrall, R. A. (1973). Diffusion-accommodated flow and superplasticity. *Acta Metallurgica*, *21*(2), 149–163. https://doi.org/10.1016/0001-6160(73)90057-6

3. Avila, G., Fernández, J. M., Maté, B., Tejeda, G., & Montero, S. (1999). Ro-vibrational Raman Cross Sections of Water Vapor in the OH Stretching Region. *Journal of Molecular Spectroscopy*, *196*(1), 77–92. https://doi.org/10.1006/jmsp.1999.7854

4. Beeler, N. M. (2006). Inferring earthquake source properties from laboratory observations and the scope of lab contributions to source physics. In R. Abercrombie, A. McGarr, H. Kanamori, & G. Di Toro (Eds.), *Geophysical Monograph Series* (Vol. 170, pp. 99–119). American Geophysical Union. https://doi.org/10.1029/170GM12

5. Billi, Andrea & Di Toro, Giulio. (2008). Fault-related carbonate rocks and earthquake indicators: Recent advances and future trends. Structural Geology: New Research. 63-86.

6. Buehn, B., Rankin, A. H., Radtke, M., Haller, M., & Knoechel, A. (1999). Burbankite, a (Sr, REE, Na, Ca)-carbonate in fluid inclusions from carbonatite-derived fluids; identification and characterization using laser Raman spectroscopy, SEM-EDX, and synchrotron micro-XRF analysis. *American Mineralogist*, *84*(7–8), 1117–1125. https://doi.org/10.2138/am-1999-7-814

7. Chen, J., Chen, J., & Yao, L. (2023). Frictional strength, electrical conductivity, and microstructure of calcite–graphite mixtures sheared at a subseismic slip rate. *Tectonophysics*, *868*, 230085. https://doi.org/10.1016/j.tecto.2023.230085

8. Collettini, C., Viti, C., Tesei, T., & Mollo, S. (2013). Thermal decomposition along natural faults during earthquakes. *Geology*, *41*, 11508. https://doi.org/10.1130/G34421.1

9. Cornelio, C., Aretusini, S., Spagnuolo, E., Di Toro, G., & Cocco, M. (2024). Multiple Seismic Slip-Rate Pulses and Mechanical and Textural Evolution of Calcite-Bearing Fault Gouges. *Journal of Geophysical Research: Solid Earth*, *129*(7), e2024JB029099. https://doi.org/10.1029/2024JB029099

10. Cornelio, C., Spagnuolo, E., Aretusini, S., Nielsen, S., Passelègue, F., Violay, M., Cocco, M., & Di Toro, G. (2022). Determination of Parameters Characteristic of Dynamic Weakening Mechanisms During Seismic Faulting in Cohesive Rocks. *Journal of Geophysical Research: Solid Earth*, *127*(7), e2022JB024356. https://doi.org/10.1029/2022JB024356

11. De Paola, N., Holdsworth, R. E., Viti, C., Collettini, C., & Bullock, R. (2015). Can grain size sensitive flow lubricate faults during the initial stages of earthquake propagation. *Earth and Planetary Science Letters*, *431*, 48–58. https://doi.org/10.1016/j.epsl.2015.09.002

12. Delle Piane, C., Clennell, M. B., Keller, J. V. A., Giwelli, A., & Luzin, V. (2017). Carbonate hosted fault rocks: A review of structural and microstructural characteristic with implications for seismicity in the upper crust. *Journal of Structural Geology*, *103*, 17–36. https://doi.org/10.1016/j.jsg.2017.09.003

13. Demurtas, M., Fondriest, M., Balsamo, F., Clemenzi, L., Storti, F., Bistacchi, A., & Di Toro, G. (2016). Structure of a normal seismogenic fault zone in carbonates: The Vado di Corno Fault, Campo Imperatore, Central Apennines (Italy). *Journal of Structural Geology*, *90*, 185–206. https://doi.org/10.1016/j.jsg.2016.08.004

14. Demurtas, M., Smith, S. A. F., Prior, D. J., Brenker, F. E., & Di Toro, G. (2019). Grain Size Sensitive Creep During Simulated Seismic Slip in Nanogranular Fault Gouges: Constraints From Transmission Kikuchi Diffraction (TKD). *Journal of Geophysical Research: Solid Earth*, *124*(10), 10197–10209. https://doi.org/10.1029/2019JB018071

15. Demurtas, M., Smith, S. A. F., Prior, D. J., Spagnuolo, E., & Di Toro, G. (2019). Development of crystallographic preferred orientation during cataclasis in low-temperature carbonate fault gouge. *Journal of Structural Geology*, *126*, 37–50. https://doi.org/10.1016/j.jsg.2019.04.015

16. Demurtas, M., Smith, S. A. F., Spagnuolo, E., & Di Toro, G. (2021). Frictional properties and microstructural evolution of dry and wet calcite–dolomite gouges. *Solid Earth*, *12*(3), 595–612. https://doi.org/10.5194/se-12-595-2021

17. Di Toro, G., Han, R., Hirose, T., De Paola, N., Nielsen, S., Mizoguchi, K., Ferri, F., Cocco, M., & Shimamoto, T. (2011). Fault lubrication during earthquakes. *Nature*, *471*(7339), 494–498. https://doi.org/10.1038/nature09838

18. Di Toro, G., Hirose, T., Nielsen, S., & Shimamoto, T. (2006). Relating high-velocity rock-friction experiments to coseismic slip in the presence of melts. In R. Abercrombie, A. McGarr, H. Kanamori, & G. Di Toro (Eds.), *Geophysical Monograph Series* (Vol. 170, pp. 121–134). American Geophysical Union. https://doi.org/10.1029/170GM13

19. Di Toro, G., Niemeijer, A., Tripoli, A., Nielsen, S., Di Felice, F., Scarlato, P., Spada, G., Alessandroni, R., Romeo, G., Di Stefano, G., Smith, S., Spagnuolo, E., & Mariano, S. (2010). From field geology to earthquake simulation: A new state-of-the-art tool to investigate rock friction during the seismic cycle (SHIVA). *RENDICONTI LINCEI*, *21*(S1), 95–114. https://doi.org/10.1007/s12210-010-0097-x

20. Di Toro, G., Pennacchioni, G., & Nielsen, S. (2009). *Fault zone properties and earthquake rupture dynamics* (pp. 87–133).

21. Durand, C., Baumgartner, L. P., & Marquer, D. (2015). Low melting temperature for calcite at 1000 bars on the join $CaCO_3$-H_2O – some geological implications. *Terra Nova*, *27*(5), 364–369. https://doi.org/10.1111/ter.12168

22. Fialko, Y., & Khazan, Y. (2005). Fusion by earthquake fault friction: Stick or slip? *Journal of Geophysical Research: Solid Earth*, *110*(B12), 2005JB003869. https://doi.org/10.1029/2005JB003869

23. Han, R., Shimamoto, T., Hirose, T., Ree, J.-H., & Ando, J. (2007). Ultralow Friction of Carbonate Faults Caused by Thermal Decomposition. *Science*, *316*(5826), 878–881. https://doi.org/10.1126/science.1139763

24. Hirose, T., & Shimamoto, T. (2005). Growth of molten zone as a mechanism of slip weakening of simulated faults in gabbro during frictional melting. *Journal of Geophysical Research: Solid Earth*, *110*(B5), 2004JB003207. https://doi.org/10.1029/2004JB003207

25. Holmi, J. T., & Lipsanen, H. (2022). WITio: A MATLAB data evaluation toolbox to script broader insights into big data from WITec microscopes. *SoftwareX*, *18*, 101009. https://doi.org/10.1016/j.softx.2022.101009

26. Hope, G. A., Woods, R., & Munce, C. G. (2001). Raman microprobe mineral identification. *Minerals Engineering*, *14*(12), 1565–1577. https://doi.org/10.1016/S0892-6875(01)00175-3

27. Kanamori, H., & Brodsky, E. E. (2004). The physics of earthquakes. *Reports on Progress in Physics*, *67*(8), 1429–1496.https://doi.org/10.1088/0034-4885/67/8/R03

28. Kuo, L.-W., Di Felice, F., Spagnuolo, E., Di Toro, G., Song, S.-R., Aretusini, S., Li, H., Suppe, J., Si, J., & Wen, C.-Y. (2017). Fault gouge graphitization as evidence of past seismic slip. *Geology*, *45*(11), 979–982. https://doi.org/10.1130/G39295.1

29. Kuo, L.-W., Li, H., Smith, S. A. F., Di Toro, G., Suppe, J., Song, S.-R., Nielsen, S., Sheu, H.-S., & Si, J. (2014). Gouge graphitization and dynamic fault weakening during the 2008 Mw 7.9 Wenchuan earthquake. *Geology*, *42*(1), 47–50. https://doi.org/10.1130/G34862.1

30. Lobanov, S. S., Dong, X., Martirosyan, N. S., Samtsevich, A. I., Stevanovic, V., Gavryushkin, P. N., Litasov, K. D., Greenberg, E., Prakapenka, V. B., Oganov, A. R., & Goncharov, A. F. (2017). Raman spectroscopy and x-ray diffraction of sp 3 CaCO3 at lower mantle pressures. *Physical Review B*, *96*(10), 104101. https://doi.org/10.1103/PhysRevB.96.104101

31. Ma, S., Shimamoto, T., Yao, L., Togo, T., & Kitajima, H. (2014). A rotary-shear low to high-velocity friction apparatus in Beijing to study rock friction at plate to

seismic slip rates. *Earthquake Science*, *27*(5), 469–497. https://doi.org/10.1007/s11589-014-0097-5

32. Miller, S. A., Collettini, C., Chiaraluce, L., Cocco, M., Barchi, M., & Kaus, B. J. P. (2004). Aftershocks driven by a high-pressure CO2 source at depth. *Nature*, *427*(6976), 724–727. https://doi.org/10.1038/nature02251

33. Mitchell, T. M., Smith, S. A. F., Anders, M. H., Di Toro, G., Nielsen, S., Cavallo, A., & Beard, A. D. (2015). Catastrophic emplacement of giant landslides aided by thermal decomposition: Heart Mountain, Wyoming. *Earth and Planetary Science Letters*, *411*, 199–207. https://doi.org/10.1016/j.epsl.2014.10.051

34. Nielsen, S., Spagnuolo, E., Violay, M., & Di Toro, G. (2021). Thermal Weakening Friction During Seismic Slip: Experiments and Models With Heat Sources and Sinks. *Journal of Geophysical Research: Solid Earth*, *126*(5), e2020JB020652. https://doi.org/10.1029/2020JB020652

35. Nielsen, S., Spagnuolo, E., Violay, M., Smith, S., Di Toro, G., & Bistacchi, A. (2016). G: Fracture energy, friction and dissipation in earthquakes. *Journal of Seismology*, *20*(4), 1187–1205. https://doi.org/10.1007/s10950-016-9560-1

36. Niemeijer, A., Di Toro, G., Nielsen, S., & Di Felice, F. (2011). Frictional melting of gabbro under extreme experimental conditions of normal stress, acceleration, and sliding velocity. *Journal of Geophysical Research*, *116*(B7), B07404. https://doi.org/10.1029/2010JB008181

37. Nissen, E., Tatar, M., Jackson, J. A., & Allen, M. B. (2011). New views on earthquake faulting in the Zagros fold-and-thrust belt of Iran: Earthquake faulting in the Zagros. *Geophysical Journal International*, *186*(3), 928–944. https://doi.org/10.1111/j.1365-246X.2011.05119.x

38. Oohashi, K., Han, R., Hirose, T., Shimamoto, T., Omura, K., & Matsuda, T. (2014). Carbon-forming reactions under a reducing atmosphere during seismic fault slip. *Geology*, *42*(9), 787–790. https://doi.org/10.1130/G35703.1

39. Oohashi, K., Hirose, T., & Shimamoto, T. (2011). Shear-induced graphitization of carbonaceous materials during seismic fault motion: Experiments and possible

implications for fault mechanics. *Journal of Structural Geology*, *33*(6), 1122–1134. https://doi.org/10.1016/j.jsg.2011.01.007

40. Osinski, G. R., & Spray, J. G. (2001). Impact-generated carbonate melts: Evidence from the Haughton structure, Canada. *Earth and Planetary Science Letters*, *194*(1–2), 17–29. https://doi.org/10.1016/S0012-821X(01)00558-1

41. Passelègue, F. X., Aubry, J., Nicolas, A., Fondriest, M., Deldicque, D., Schubnel, A., & Di Toro, G. (2019). From fault creep to slow and fast earthquakes in carbonates. *Geology*, *47*(8), 744–748. https://doi.org/10.1130/G45868.1

42. Pozzi, G., De Paola, N., Nielsen, S. B., Holdsworth, R. E., Tesei, T., Thieme, M., & Demouchy, S. (2021). Coseismic fault lubrication by viscous deformation. *Nature Geoscience*, *14*(6), 437–442. https://doi.org/10.1038/s41561-021-00747-8

43. Rempe, M., Di Toro, G., Mitchell, T. M., Smith, S. A. F., Hirose, T., & Renner, J. (2020). Influence of Effective Stress and Pore Fluid Pressure on Fault Strength and Slip Localization in Carbonate Slip Zones. *Journal of Geophysical Research: Solid Earth*, *125*(11), e2020JB019805. https://doi.org/10.1029/2020JB019805

44. Rempe, M., Mitchell, T. M., Renner, J., Smith, S. A. F., Bistacchi, A., & Di Toro, G. (2018). The Relationship Between Microfracture Damage and the Physical Properties of Fault-Related Rocks: The Gole Larghe Fault Zone, Italian Southern Alps. *Journal of Geophysical Research: Solid Earth*, *123*(9), 7661–7687. https://doi.org/10.1029/2018JB015900

45. Rempe, M., Smith, S. A. F., Ferri, F., Mitchell, T. M., & Di Toro, G. (2014). Clast-cortex aggregates in experimental and natural calcite-bearing fault zones. *Journal of Structural Geology*, *68*, 142–157. https://doi.org/10.1016/j.jsg.2014.09.007

46. Rempe, M., Smith, S., Mitchell, T., Hirose, T., & Di Toro, G. (2017). The effect of water on strain localization in calcite fault gouge sheared at seismic slip rates. *Journal of Structural Geology*, *97*, 104–117. https://doi.org/10.1016/j.jsg.2017.02.007

47. Rividi, N., Van Zuilen, M., Philippot, P., Ménez, B., Godard, G., & Poidatz, E. (2010). Calibration of Carbonate Composition Using Micro-Raman Analysis: Application to

Planetary Surface Exploration. *Astrobiology*, *10*(3), 293–309. https://doi.org/10.1089/ast.2009.0388

48. Schmid, T., & Dariz, P. (2015). Shedding light onto the spectra of lime: Raman and luminescence bands of CaO, Ca(OH) $_2$ and CaCO $_3$. *Journal of Raman Spectroscopy*, *46*(1), 141–146. https://doi.org/10.1002/jrs.4622

49. Scholz, C. H. (2002). *The Mechanics of Earthquakes and Faulting* (2nd ed.). Cambridge University Press. https://doi.org/10.1017/CBO9780511818516

50. Scholz, C. H. (2019). *The Mechanics of Earthquakes and Faulting* (3rd ed.). Cambridge University Press. https://doi.org/10.1017/9781316681473

51. Sibson, R. H. (1975). Generation of Pseudotachylyte by Ancient Seismic Faulting. *Geophysical Journal International*, *43*(3), 775–794. https://doi.org/10.1111/j.1365-246X.1975.tb06195.x

52. Siman-Tov, S., Aharonov, E., Sagy, A., & Emmanuel, S. (2013). Nanograins form carbonate fault mirrors. *Geology*, *41*(6), 703–706. https://doi.org/10.1130/G34087.1

53. Smith, S. A. F., Di Toro, G., Kim, S., Ree, J.-H., Nielsen, S., Billi, A., & Spiess, R. (2013). Coseismic recrystallization during shallow earthquake slip. *Geology*, *41*(1), 63–66. https://doi.org/10.1130/G33588.1

54. Smith, S. A. F., Nielsen, S., & Di Toro, G. (2015). Strain localization and the onset of dynamic weakening in calcite fault gouge. *Earth and Planetary Science Letters*, *413*, 25–36. https://doi.org/10.1016/j.epsl.2014.12.043

55. Spagnuolo, E., Plümper, O., Violay, M., Cavallo, A., & Di Toro, G. (2015). Fast-moving dislocations trigger flash weakening in carbonate-bearing faults during earthquakes. *Scientific Reports*, *5*(1), 16112. https://doi.org/10.1038/srep16112

56. Tlili, M. M., Amor, M. B., Gabrielli, C., Joiret, S., Maurin, G., & Rousseau, P. (2002). Characterization of CaCO $_3$ hydrates by micro-Raman spectroscopy. *Journal of Raman Spectroscopy*, *33*(1), 10–16. https://doi.org/10.1002/jrs.806

57. Tsutsumi, A., & Shimamoto, T. (1997). High-velocity frictional properties of gabbro. *Geophysical Research Letters*, *24*(6), 699–702. https://doi.org/10.1029/97GL00503

58. Urashima, S., Morita, M., Komatani, S., & Yui, H. (2023). Non-destructive estimation of the cation composition of natural carbonates by micro-Raman spectroscopy. *Analytica Chimica Acta*, *1242*, 340798. https://doi.org/10.1016/j.aca.2023.340798

59. Violay, M., Nielsen, S., Gibert, B., Spagnuolo, E., Cavallo, A., Azais, P., Vinciguerra, S., & Di Toro, G. (2014). Effect of water on the frictional behavior of cohesive rocks during earthquakes. *Geology*, *42*(1), 27–30. https://doi.org/10.1130/G34916.1

60. Violay, M., Nielsen, S., Spagnuolo, E., Cinti, D., Di Toro, G., & Di Stefano, G. (2013). Pore fluid in experimental calcite-bearing faults: Abrupt weakening and geochemical signature of co-seismic processes. *Earth and Planetary Science Letters*, *361*, 74–84. https://doi.org/10.1016/j.epsl.2012.11.021

61. Wyllie, P. J. (1965). Melting Relationships in the System CaO-MgO-CO2-H2O, with Petrological Applications. *Journal of Petrology*, *6*(1), 101–123. https://doi.org/10.1093/petrology/6.1.101

62. Wyllie, P. J., & Huang, W.-L. (1976). Carbonation and melting reactions in the system CaO?MgO?SiO2?CO2 at mantle pressures with geophysical and petrological applications. *Contributions to Mineralogy and Petrology*, *54*(2), 79–107. https://doi.org/10.1007/BF00372117

Acknowledgments

Acknowledging the completion of this thesis, I reflect not only on the academic achievement but on the personal journey that has shaped me through these years. This work would not have been possible without the immense support, guidance, and encouragement I received from so many people.

I am deeply grateful to my family for their unwavering support throughout this journey. To my love, Kimia, thank you for your endless inspiration and strength.

I owe a special thanks to my supervisor, Professor Giulio Di Toro, whose expert guidance and mentorship went far beyond the typical supervisory role. I also extend my sincere appreciation to Stefano Aretusini and Elena Spagnuolo for their invaluable support during my experiments and writing this thesis.

I am also deeply indebted to Rodrigo De Aguilera for his expertise and unwavering support, and to Jacopo Nava for his crucial assistance.

Finally, to my friends, thank you for the camaraderie and shared experiences.

With deepest gratitude,

Kamyar Tamizkar